Volume 9
Number 1
7 January 2018
Pages 1-268

Chemical Science

rsc.li/chemical-science

ISSN 2041-6539

EDGE ARTICLE
Xinjing Tang et al.
Caged circular siRNAs for photomodulation of gene
expression in cells and mice

ROYAL SOCIETY
OF CHEMISTRY

ROYAL SOCIETY
OF CHEMISTRY

rsc.li/chemical-science

ARTICLE

Emission-tunable manganese(II) halides: structure-property relationships and functional applications

Chuying Wang, [a] Yacong Li [a] and Zhengtao Deng *[a]

Luminescent Mn(Ⅱ) complexes have attracted extensivrly attention owing to their properties of color tunable, high PLQY, large stokes shift and thermal stability. Luminescent Mn(Ⅱ) complexes can exhibit orange, green, and red emissions depending on the environment of Mn^{2+}. These various properties made Mn(Ⅱ) complexes attractive candidates in different fields of applications such as LEDs and radiation detection. In this perspective, we connect the emissions of Mn(Ⅱ) complexes with the corresponding crystal structure and the environment of Mn^{2+}. Then we summarized recent progress of luminescent Mn(Ⅱ) complexes on LEDs and radiation detections. Finally, we express challenge and outlook for future researches on luminescent Mn(II) complexes.

1 Introduction

In the past few years, lead halide perovskites have become promising materials for optoelectronic devices due to their excellent optoelectronic properties.[1, 2] However, their toxicity and poor stability have hindered further in many fields.[3] One of the most effective solution is to find nontoxic and reliable alternatives beyond lead halide perovskite.[4-6] Mn(Ⅱ) halides have emerged as sustainable alternatives to lead perovskites, achieving near-unity photoluminescence quantum yield (PLQY) and enabling emission tunability to green and red luminescence through structural control. These earth-abundant systems combine luminescence efficiency with environmental compatibility, addressing demands for eco-friendly photoelectric applications.

The intrinsic luminescence of manganese halides originates from d-d electronic transitions of the manganese center, where the crystal field splitting determines emission characteristics through ligand field modulation. Manganese first emerged as strategic luminescent dopants for host material with low PLQY, where its distinct electronic configuration enables efficient energy transfer pathways for photoluminescence enhancement. The synthesized Mn-doped ZnS nanocrystals (NCs) by Bhargava in 1994 are the earliest semiconductor NCs, exhibiting quantum yield less than 20%[7]. Mn^{2+} dopants in II-VI semiconductors (e.g., ZnS, CdSe) achieve tetrahedral coordination through isovalent substitution, activating spin-forbidden d-d photoluminescence via crystal field engineering[8]. Since then, a great diversity of Mn-doped II–VI semiconductor NCs have been explored and applied

to biomedical imaging[9], white light emitting diodes[10], solar cells[11], radiation detection[12] and luminescent solar concentrators[13]. Given that the great potential for various light emission applications of Mn-doped semiconductors NCs, metal halide perovskite NCs has been also developed as the latest semiconductor host of Mn(Ⅱ) dopant. In 2016, Mn-doped $CsPbX_3$ perovskite NCs were almost simultaneously synthesized by Parobek et al.[14] and Liu et al.[15] via modified hot injection process.

Besides of dopant, Mn can also be applied as independent luminescent center without doping. Luminescent Mn(Ⅱ) halide complexes, as one of emerging lead free materials, have been intensively investigated over the past decades owing to their properties of tunable emission, high PLQY, large stokes shift, good thermal stability and low toxic nature compared to lead halide perovskites. In recent years, various luminescent Mn(Ⅱ) halide complexes have been designed and synthesized. According to the coordination environment of center Mn^{2+}, Mn(Ⅱ) halides can be classified to four fold-coordinated $[MnX_4]^{2-}$ and six fold-coordinated $[MnX_6]^{4-}$ manganese halide complexes. Through the emission wavelength, Mn(Ⅱ) halides can be classified to green and red Mn(Ⅱ) phosphors. By their crystal structure, Mn(Ⅱ) complexes are further classified in zero-, one- and two-dimensional structures. The diversity of Mn(Ⅱ) halide complexes leads to their different photoelectric properties, which can be applied in different fields. For example, Ju et al. fabricate white LED (WLED) exhibiting luminous efficacy to 96 lm W^{-1} by green $(C_5H_6N)_2MnBr_4$ and red $C_5H_6NMnCl_3$ phosphors on blue chip, reflecting high PLQY and good thermal stability of these manganese(II) complexes.[16] Wang et al. prepared pure red LED with $(ABI)_4MnBr_6$ showing the maximum recording brightness of 4700 cd m^{-2} and EQE of 9.8%, suggesting the excellent electroluminescence (EL) performance of this complex.[17] Besides of LED, Mn(Ⅱ) complexes can also be applied to radiation detention. Mn-doped $(C_{18}H_{37}NH_3)_2PbBr_4$ scintillator was finally made into

a. College of Engineering and Applied Sciences, State Key Laboratory of Analytical Chemistry for Life Science, National Laboratory of Micro-structures, Nanjing University, Nanjing, Jiangsu, 210023, P. R. China. E-mail: dengz@nju.edu.cn

† Electronic Supplementary Information (ESI) available: [details of any supplementary information available should be included here]. See DOI: 10.1039/x0xx00000x

imaging plates for fast neutron radiography with 0.5 lp/mm spatial resolution.[18] Ma et al. synthesized X-ray scintillation with a high light yield of 80,000 photon MeV^{-1}, and a low detection limit of 72.8 nGy s^{-1} with $(C_{38}H_{34}P_2)MnBr_4$, expressing the potential of manganese(II) complexes on X-ray imaging.[19]

According to previous researches, the emission of Mn from both dopant and Mn(II) halide complexes both from $^4T_1(G) \rightarrow ^6A_1(S)$ transition of Mn^{2+}. The environment of Mn^{2+} in different structures leads to different performance of the luminescent properties. In this perspective, we have summarized recent progresses on luminescent Mn(II) complexes. We relate the luminescent properties of Mn(II) complexes to their corresponding environment and crystal structures. Then we discuss their applications on LEDs and X-ray imaging. Finally, we express an outlook for the future development for Mn(II) halides.

2 Structures and properties of Mn halides

2.1 Emission of Mn-doped perovskite NCs

The electronic structure of Mn^{2+} in crystalline environments was analyzed through Tanabe-Sugano theory, incorporating electron correlations and crystal field (CF) effects[20]. Cubic CF splitting partially lifts degeneracies of the ^4G, ^4P, and ^4D terms, generating distinct $^4T_1(G)$, $^4T_2(G)$, $^4A_1(G)$, $^4E(G)$, $^4T_2(D)$, $^4E(D)$, and $^4T_1(P)$ states, which will be discussed in chapter 2.3 and 2.2 in detailed. Mn^{2+} photoluminescence originates from the $^4T_1(G) \rightarrow ^6A_1(S)$ transition within visible wavelengths[21-23]. The emission energy dependence on the CF strength, enabling chromatic tuning across host matrices via ligand field engineering.

For Mn as dopant, manganese (II) ions are incorporated into metal halide hosts through substitutional doping strategies, where their luminescent activation emerges from coordination-tuned crystal field splitting. The emission characteristics are governed by the ligand-field symmetry coordination environment of the host. For instance, Mn^{2+} substitution in tetrahedral $[ZnX_4]^{2-}$ units yields green emission under Td-symmetry crystal field splitting[24, 25], while octahedral coordination in $[CdCl_6]^{4-}$ environments generates distinct red luminescence through Oh-symmetry crystal field effects[26].

Recently, Mn^{2+} doped $CsPbCl_3$ perovskites exhibit tunable dual-band emission through structural confinement-mediated energy transfer, enabling applications in white-light-emitting diodes (WLEDs)[27], luminescent solar concentrators (LSCs)[28], and anti-counterfeiting[29] technologies. Figure 1a show that Mn-doped $CsPbCl_3$ NCs have a distinct dual emission behavior consisting of a narrow PL band at ~ 400 nm (blue – violet) and a broad PL band at ~ 600 nm (yellow - orange emission). The former is generally attributed to host band edge exciton recombination, the latter to ligand field transition ($^4T_1(G) \rightarrow ^6A_1(S)$) of Mn^{2+} ions. Since the transition is spin-forbidden, the Mn dopant luminescence in perovskite NCs is accompanied by a microsecond or millisecond lifetime, consistent with Mn-doped II–VI semiconductor NCs.[30]

2.1.1 Bandgap-dependent PL of Mn-doped perovskite NCs

The emission of Mn-doped $CsPbX_3$ perovskite NCs is host bandgap-dependent. Figure 1b depicts the energy levels alignment of $CsPbX_3$ perovskite and Mn^{2+} ions d-state. In case of Mn-doped $CsPbCl_3$ NCs, photo-generated exciton has the highest band gap energy and favour the forward energy transfer from band edge to Mn^{2+} excited state, which is ultimately contributed to the introduction of Mn^{2+} ions radiative pathway.[15] However, the gap energy of Br-based or I-based perovskite NCs is close to Mn^{2+} excited state and hinders the energy transfer process, resulting in inefficient dopant emission was observed in Mn-doped $CsPbBr_3$ and $CsPbI_3$ NCs.[31, 32] Fortunately, quantum confinement effect provides a new chance for obtaining Mn emission in non Cl-based perovskite NCs. For example, Parobek et al directly synthesized dual-emission $CsPbBr_3$ nanocubes (6.5 nm) and nanoplatelets (NPLs, thickness 2 nm) with confinement size (7 nm) via the pre-formation of $A_2[Pb_{1-x}Mn_x]Br_4$ (A=alkylammonium).[31] The interesting thing is that dopant emission dominate in Mn-doped $CsPbBr_3$ NPLs, in contrast to stronger host emission in Mn-doped $CsPbBr_3$ nanocubes, indicating that more stable exciton-dopant exchange interaction due to enhance confinement effect in NPLs. Furthermore, Wang et al. first reported the hot electrons up-conversion process in quantum confined Br-based perovskite NCs and NPLs.[33] As is shown in Figure 1c, hot electrons are generated by the Auger energy transfer from excited Mn^{2+} ions to another exciton. When energy exceeds the threshold, hot electrons can long-range transfer and improve the catalytic efficiency.[34]

2.1.2 Concentration-dependent PL of Mn-doped perovskite NCs

Mn^{2+} ions doping concentration is also capable of tailoring the emission of Mn-doped $CsPbX_3$ perovskite NCs. Liu et al. synthesized $CsPb_xMn_{1-x}Cl_3$ perovskite NCs through adding excess $MnCl_2$ dopant into the solution and elevated the temperature, where Mn dopant emission was tuned from 569 nm to 587 nm with the increase of doping concentration from 3% to 46%.[35] The red shift of Mn dopant emission was attributed to enhanced Mn^{2+} - Mn^{2+} interaction, which come under observation in most Mn-doped system.[36-40] In addition, as the doping concentration increases, the PLQYs of Mn-doped $CsPbCl_3$ perovskite NCs first rises then descends. A plausible explanation is that there is an optimal Mn doping concentration in $CsPbCl_3$ perovskite NCs, which not only can ensure enough Mn^{2+} ions to compete with the exciton recombination and yield intense Mn emission, but also fail to cause serious PL quenching by forming $Mn^{2+}-Mn^{2+}$ pairs, nonradiative defects and deformation of the crystal structure at high Mn doping.[41] Therefore, numerous efforts have been focused on controlling doping concentration and improving PLQYs of Mn-doped $CsPbCl_3$ perovskite NCs.[35, 40-45]

2.1.3 Improved doping and emission efficiency

At present, the majority of Mn-doped $CsPbX_3$ perovskite NCs are synthesized via modified hot injection approach by Protesescu et al.[46] Figure 1d presents the typical process, Mn-doped perovskite NCs form after injecting Cs-oleate into a solution containing metal halide salts ($PbCl_2$ and $MnCl_2$). However, metal halide salts are low solubility in the nonpolar solvent,[47] thus resulting in low doping efficiency (Table 1).

Moreover, since the ratio of cations to anions is fixed at stoichiometric ratio of metal halide salts, it is not possible to precisely tune the composition of Mn-doped perovskite NCs. In particular, it is difficult to create an environment with rich halide ions, which has been proved to favour the formation of Mn-doped $CsPbX_3$ perovskite NCs with highly stability and improved PLQY.[48-51] To promote doping and emission efficiency of Mn-doped $CsPbX_3$ perovskite NCs, the authors proposed a novel "two step hot injection approach" recently.[52] As is shown in Figure 1e, metal acetate salts (Pb-acetate and Mn-acetate) with good solubility in solution containing oleic acid are chosen as Pb sources and Mn sources, respectively. The first step is to inject an excessive amount of alkylamine halide salts and induce the formation of $[PbX_6]^{4-}$ clusters and $[PbX_6]^{4-}$ clusters with highly coordinated number. The second step is to inject Cs-oleate, which can make clusters grow into Mn-doped perovskite NCs. In our method, all sources are independent of each other, so the composition of the final NCs is completely controllable. More importantly, we used Mn: Pb in a 3:7 mol ratio to get 17.3% doping in cubic $CsPbCl_3$ nanocubes. In fact, metal acetate salts have been reported as unsuitable dopants, but Mn-doped $CsPbCl_3$ perovskite NCs achieved the highest 48.5% doping efficiency and 84.4% quantum efficiency at the same time via the two-step hot injection.

In luminescent Mn-doped NCs, surface states serve as critical determinants of emission behavior[53]. Under low Mn-doping conditions, $CsPbCl_3$ NCs demonstrate enhanced PL intensity with rising Mn concentrations, a behavior directly correlated with $MnCl_2$-mediated chloride vacancy passivation during colloidal synthesis[14]. However, excessive dopant incorporation induces deterioration of PLQY in Mn doped $CsPbCl_3$, which is due to the dominant Mn-Mn exchange interactions supersede exciton-to-dopant energy transfer process[40]. This fundamental competition between defect passivation and dopant-dopant coupling establishes a concentration threshold for maximizing luminescent performance.

2.2 Tetrahedral units for green emission

The green emission of Mn(Ⅱ) halide complexes originates from the tetrahedral coordinated Mn(Ⅱ) units, which is mostly $[MnX_4]^{2-}$ (X=Cl, Br, I) for Mn(Ⅱ) halide complexes. Tetrahedral coordinated Mn(Ⅱ) exhibits green emission and the emission of Mn(Ⅱ) tetrahedral (T_d) crystal fields has been studied for decades.[54] In a Mn(Ⅱ) T_d field with oxide as ligands, green emission is obtained with narrow FWHM.[55, 56] However, the main drawback of oxide ligand T_d field for Mn(Ⅱ) is slow emission decay and high reaction temperature.

In 2019, Kovalenko et al. synthesized a series of T_d $[MnX_4]^{2-}$ complexes with green emission. They found that the crystal field effects and spin-orbit coupling of Mn^{2+} determine the optical properties of manganese(II) complexes such as PL peak positions, FWHM and emission decay.[57]

2.2.1 Structure of Mn(Ⅱ) halide complexes consist of tetrahedral units

The formula of $[MnX_4]^{2-}$ halide complexes are usually A_2MnX_4 or $AMnX_4$. A can be inorganic cation Cs^+[58] or organic cations such as organic ammonium[59-65] and phosphorus[19, 66, 67] groups. To

charge balance the Mn halide system, it should require two +1 cations[68] or one +2 cation[19] to push the $[MnX_4]^{2-}$ tetrahedron further apart.[62] $AMnX_4$ containing divalent A-site typically incorporates phosphonium cations (e.g., $(C_{40}H_{38}P_2)MnBr_4$[69], $(C_{38}H_{34}P_2)MnBr_4$[19], $[DMAEMP]MnCl_4$ and $[PDMIm]_2MnCl_4$[63]), crystallizing in triclinic or monoclinic systems. A_2MnX_4 derivatives with monovalent A-site cations primarily utilize ammonium cations (e.g., $(C_{10}H_{16}N)_2MnX_4$[23, 70], $(C_8H_{20}N)_2MnBr_4$[16]) or phosphonium cations (e.g., $(BzTPP)_2MnBr_4$[71], $(BuTPP)_2MnBr_4$[72]), typically adopting monoclinic symmetry. Both $AMnX_4$ and A_2MnX_4 green-emissive Mn(Ⅱ) halides exhibit zero-dimensional (0D) architectures characterized by isolated $[MnX_4]^{2-}$ tetrahedral units (Figures 2b, c).

2.2.2 Optical properties of green Mn(Ⅱ) halide complexes

Optical properties of Mn(Ⅱ) halide complexes, including PL, PLE and Abs, are derived from the d orbital of Mn(Ⅱ) in different crystal fields. As for green $[MnX_4]^{2-}$ complexes, the split of d orbit is affected by tetrahedral field as shown in Figure 2d.[57, 73] Excitation of green T_d Mn(Ⅱ) halide complexes mainly comes from two transitions: group one of lower energy of $^6A_1$ to $^4T_1(G)$, $^4T_2(G)$,$^4A_1$,$^4E(G)$ transitions and group two of higher energy of $^6A_1(S)$ to $^4T_2(D)$, $^4E(D)$, $^4T(P)$ transitions. Group of higher energy sometimes also contains $^6A_1$ to $^4T(P)$ transition. PL emission originates from the radiative recombination from $^4T_1(G) \rightarrow {}^6A_1(S)$ transition.

For example, Seshadri et al. synthesized $(TMPTA)_2MnBr_4$ exhibiting green emission at 520 nm with a PLQY of 98%.[62] The excitation spectrum features two primary transitions: $^6A_1$ to $^4T_1(G)$, $^4T_2(G)$,$^4A_1$,$^4E(G)$ (430−490 nm) and $^6A_1(S)$ to $^4T_2(D)$, $^4E(D)$, $^4T(P)$ (350−390 nm). Artem'ev et al. reported R/S-[MBA-Me_3]MnBr_4 with emission at 519 nm (PLQY = 98%),[65] where excitation corresponds to $^6A_1$ to $^4T_1(G)$, $^4T_2(G)$,$^4A_1$,$^4E(G)$ and $^6A_1(S)$ to $^4T_2(D)$, $^4E(D)$, $^4T(P)$ transitions (Figure 2e and Figure 2f).[65, 73] Similarly, Ma et al. synthesized $(C_{38}H_{34}P_2)MnBr_4$ single crystals expressing green emission (517 nm, 95%) with identical excitation characteristics.[19] The excitation spectrum has the same features as the absorption spectrum corresponding to two groups transitions of blue and UV region.

The photoluminescent properties of Mn(II) halides are governed by ligand-field splitting and spin-orbit coupling effects, which dictate emission energies and bandwidths[57]. The electron interaction between neighbouring Mn^{2+} plays an important role in the PL performance. A tendency similar to concentration quenching in Mn doped NCs is observed in Mn(Ⅱ) halides[62]. PLQY of green $[MnX_4]^{2-}$ halide complexes is related to Mn "concentration" (Figure 2a), which can be evaluated by Mn-Mn distance(Figure 3),[59, 60, 62, 63, 66, 68, 74, 75] which is interpreted as analogous to the "concentration quenching effect" in Mn^{2+}-doped inorganic phosphors[76]. As for 0D Mn(Ⅱ) complexes, the longer Mn-Mn distances weakened the nonradiative energy transfer between neighbouring Mn^{2+} centers in $[MnX_4]^{2-}$ and promoted the radiative recombination of $^4T_1(G) \rightarrow {}^6A_1(S)$ transition, achieving a higher PLQY.[63] In organic-inorganic hybrid manganese halides, photoluminescence quenching originates from nonradiative decay pathways driven by multi-phonon relaxation processes

mediated through interaction from $[MnCl_4]^{2-}$ and A-cation[77] and between Mn center and X ligands[23].

Beyond PLQY, the Stokes shift critically governs luminescent behavior in Mn(II) halides. Recent studies demonstrate that controlled tetrahedral distortion enables systematic emission tuning: Zhang et al.[78] and Qi et al.[79] achieved spectral shifts from green through yellow to red by modifying $[MnX_4]^{2-}$ distortions. This tunability arises from distortion-induced modulation of both crystal field splitting and electron-phonon coupling. Pronounced angular distortions reduce the $^4T_1(G)$-$^6A_1(S)$ energy gap. During triclinic-to-orthorhombic phase transitions, Br-Mn-Br angle alterations redshift emission to 555 nm with increasing Dq/B ratio[79].

This reflects enhanced ligand field strength and decreased $^4T_1(G)$-$^6A_1(S)$ energy separation. Distorted tetrahedra intensify lattice vibrations, broadening emission linewidths from 51 nm to 68 nm via strengthened electron-phonon coupling[80]. Crucially, bond-angle distortions dominate these spectral modifications, while bond-length variations prove negligible.[79] The pseudohalide series further confirms this mechanism: progressive tetrahedral distortion elevates dipole moments, enhancing crystal field strength and inducing correlated emission redshifts and strengthened electron-phonon coupling, inducing bandwidth broadening[78]. Thus, angular distortion constitutes a rational design strategy for tailoring Mn(II) halide emission profiles.

In summary, the photoluminescence quantum yield (PLQY) of Mn(II) halides is primarily governed by Mn-Mn interatomic distances, which control concentration quenching effects. Concurrently, the Stokes shift is modulated by angular distortion within the crystal structure, which also dictates emission peak positions. Furthermore, structural distortions and organic A-site cations[23, 26, 81, 82] influence electron-phonon coupling, determined the FWHM of luminescence.

2.3 Octahedral units for red emission

The red emission of Mn(II) complexes is derived from the six coordinated Mn(II) octahedral units, which is mostly $[MnX_6]^{4-}$ (X=Cl, Br, I) for Mn(II) halide complexes. The red emission of Mn(II) in octahedral (O_h) crystal field mainly arise from stronger ligand field compared to the green emission of Mn(II) in T_d environment.[57]

2.3.1 Structure of Mn(Ⅱ) halide complexes consist of Octahedral units

For red emissive Mn(Ⅱ) halide complexes, the emission comes from O_h $[MnX_6]^{4-}$ units as shown in Figure 4a. However, different from isolated $[MnX_4]^{2-}$ units of green emissive Mn(Ⅱ) halide complexes, $[MnX_6]^{4-}$ unit can be isolated or connect to another $[MnX_6]^{4-}$ unit. According to the connection between the O_h $[MnX_6]^{4-}$ units, structure of red emissive Mn(Ⅱ) halides is crystallized to 0D, 1D and 2D structures and the 0D structure can be further divided into isolated structure and partially connected structure.

Here we use the formula A_mMnX_n to illustrate O_h $[MnX_6]^{4-}$ red halide complexes. A is mainly +1 or +2 cation for red $[MnX_6]^{4-}$ halide complexes. For isolated 0D structure, Mn^{2+} ion is surrounded by six halide ions to form a unique $[MnX_6]^{4-}$

octahedron with formula of A_4MnX_6, as shown in Figure 4b.[17] For partially connected 0D structure, Mn^{2+} ion is encircled by six halide ions to form $[MnX_6]^{4-}$ octahedral units, then two or three $[MnX_6]^{4-}$ units further form a unique $[Mn_2X_9]^{5-}$ or $[Mn_3X_{12}]^{6-}$ unit by face-sharing (Figure 4c and Figure 4d).[61, 83] The unit is separated by +1 cation A to form 0D structure with formula of $A_{(n+3)}Mn_nX_{(3n+3)}$, where n stands for the number of $[MnX_6]^{4-}$ octahedral in face-sharing to form a unique $[Mn_nX_{3n+3}]^{(n+3)-}$ unit. 1D Mn(Ⅱ) halide structures feature $[MnX_6]^{4-}$ octahedral units where Mn^{2+} ions coordinate with six ligands. These octahedra form linear chains through face-sharing along specific crystallographic directions (Figure 4e)[16, 84-88] or via edge-sharing connection (Figure 4f) [21, 89]. Face-shared 1D assemblies adopt the general formula $AMnX_3$[85, 90], while edge-shared counterparts conform to $AMnX_3B$ (B = neutral ligands, e.g., H_2O) [21, 91]. For 2D structure, each Mn^{2+} is also surrounded by six X⁻. The $[MnX_6]^{4-}$ octahedral share corners to form the two-dimensional network with +2 cation A occupying the space enclosed by $[MnX_6]^{4-}$ octahedron (Figure 4g). In the inorganic layers, each Mn atom is surrounded by six Cl atoms, in which four equatorial Cl atoms bridge four different Mn atoms to form two-dimensional $[MnCl_4]_n^{2-}$ inorganic layers as shown in Figure 4f. [92] Thus, the formula of 2D Mn(Ⅱ) halide complexes is $AMnX_4$ with +2 A cation.

The d-d transition of Mn^{2+} in the centrosymmetric octahedral crystal field (O_h) is forbidden by the Laporte selection rule, leading to a low PLQY.[57] Thus, distortion of $[MnX_6]^{4-}$ octahedrons in structure is necessary for red emissive Mn(Ⅱ) halide complexes to achieve superior luminescence performance. Due to the diversity crystal structure, luminescent properties of red manganese halides are more complex than that of green manganese halides.

2.3.2 Optical properties of red Mn(Ⅱ) halide complexes

Similar to tetrahedral $[MnX_4]^{2-}$ complexes, the optical properties of octahedral $[MnX_6]^{4-}$ systems arise from d-orbital splitting in O_h symmetry (Figure 4h).[73] Excitation involves three characteristic energy regions: the lowest-energy $^6A_1(S)$ to $^4T_1(G)$ transition in the green region, intermediate $^6A_1(S)$ to $^4T_2(G)$,$^4A_1$,$^4E(G)$ transition, transitions in blue, and higher-energy $^6A_1(S)$ to $^4T_2(D)$, $^4E(D)$, $^4T(P)$ transitions. Emission consistently originates from the $^4T_1(G)$ to $^6A_1(S)$ radiative transition (Figure 4h, i).

This excitation-emission scheme persists across diverse structures: Wang et al. synthesized isolated 0D $(ABI)_4MnBr_6$ (629 nm, 80%), [17] with excitations at $^6A_1(S)$ to $^4T_1(G)$, $^4T_2(G)$,$^4A_1$,$^4E(G)$ (525 nm, 374nm and 440 nm) and $^6A_1(S)$ to $^4T_2(D)$, $^4E(D)$ (340 nm and 365 nm). Wu et al. reported partially connected 0D $(Gua)_2MnCl_4$ (650 nm, 76%) with similar excitations[83]. Ju et al. demonstrated equivalent transitions in 1D $C_4H_{12}NMnCl_3$ (635 nm, 91.8%)[16].

The distinct photoluminescent properties of green- and red-emissive Mn(II) halide complexes fundamentally arise from differences in crystal field splitting within tetrahedral T_d $[MnX_4]^{2-}$ and octahedral O_h $[MnX_6]^{4-}$ coordination environments, governing both excitation and emission characteristics.[16, 73, 77] The associated Stokes shift between $^6A_1(S)$ to $^4T_1(G)$ excitation and $^4T_1(G)$ to $^6A_1(S)$ emission further correlates with these

distinct geometries.[77] While Mn-Mn interatomic distances influence the photoluminescence quantum yield (PLQY) of six-coordinate Mn(II) halides by mitigating concentration quenching[93], the luminescence efficiency in red-emitting systems is more critically governed by octahedral distortion, as mandated by the Laporte selection rule.

For instance, comparing 0D red manganese halides: $(ABI)_4MnBr_6$ achieves 80% PLQY (Mn-Mn > 8.74 Å)[17], comparing to $(Gua)_2MnCl_4$ (76%, 8.551 Å)[83] and $CsMnCl_3$ (42%, 4.1 Å)[94]. However, due to the divisive crystal structure of red manganese halides, the "concentration" of Mn is not a reliable parameter[76]. Different from green manganese halides, the Mn-Mn distance in red manganese halides is not the main influence parameter. Paradoxically, 1D $CsMnCl_3$ exhibits a longer nearest Mn-Mn distance (4.1 Å) yet lower PLQY (42%)[94] than $(TMSO)MnCl_3$ (3.24 Å, 86%)[90] and $(C_9H_{17}NO_2)[MnCl_3]$ (3.213 Å, 67%)[86] (Table 2), demonstrating that Mn-Mn distance exerts a comparatively minor influence on PLQY in red-emitting systems due to the Laporte selection rule. Furthermore, the significant PLQY difference between $(CH_3)_4NMnCl_3$ (94%) and $(CH_6N_3)_2MnCl_4$ (69%)[85] underscores the dominant role of distortion. As displayed in Table 2 and Figure 5, high-PLQY red Mn halides consistently exhibit elevated bond-length (Δd) or bond-angle (Δθ) distortion parameters (defined below), contrasting with green emitters where Mn-Mn distance is paramount. This highlights the critical constraint of the Laporte rule on six-coordinate Mn(II) luminescence, necessitating significant focus on structural distortion.

$$\Delta d^2 = \frac{1}{6}\sum_{i=2}^{6}\left[\frac{(d_i - d_{ave})}{d_{ave}}\right]^2 \qquad \text{eq1}$$

$$\Delta \theta^2 = \frac{1}{12}\sum_{i=1}^{12}\left[\frac{(\theta_i - 90^o)}{90^0}\right]^2 \qquad \text{eq2}$$

where d_{ave} is the average Mn–Br bond lengths and d_i is the individual Mn–X (X=Cl, Br or O) bond length, θ_i is a single Br–Mn–Br bond angle.

Compounds incorporating Mn-O bonds from H_2O ligands exhibit markedly higher Δd and Δθ values yet significantly reduced PLQY, warranting separate analysis of hydrated and anhydrous systems. To assess octahedral distortion, we introduce the composite parameter Δd·Δθ. PLQY exhibits no monotonic dependence on Δd or Δθ alone (Table 2, Figure 5a). For example, $(TMSO)MnCl_3$ showed higher PLQY (86%)[90] despite lower Δd (0.0069 Å) than $CsMnCl_3$ (42%, 0.0074 Å)[94]. Similarly, $(ABI)_4MnCl_6$ exhibited higher PLQY (99%)[82] despite but lower Δθ (3.5°) than $(C_9H_{17}NO_2)MnCl_3$[86]. PLQY for red Mn halides demonstrates a monotonic increase with the composite distortion parameter Δd·Δθ (Figure 5b). Although hydrated compounds exhibit greater distortion, their PLQY is consistently lower, attributed to detrimental perturbations of the crystal field by O ligands. Furthermore, water-mediated structure regulation can introduce potential emission instability, causing luminescence fluctuations.

Therefore, achieving stable, high-efficiency red emission necessitates the use of anhydrous, halide-coordinated Mn(II) systems, where optimized octahedral distortion maximizes radiative efficiency within the constraints of the Laporte rule.

2.4 Structure regulation between red and green emission

Emission mainly depends on the T_d and O_h ligand field of Mn^{2+}, thus changing of the coordination environment of Mn^{2+} can influence the optical properties of Mn(II) halide complexes. For Mn(II) halide complexes with same components, changing coordination geometry around Mn^{2+} from four fold-coordinated $[MnX_4]^{2-}$ to six fold $[MnX_6]^{4-}$ achieve emission from green to red.[73, 91] Furthermore, besides of halides, O also participates in the crystal field according to Mn-O bonding and change the coordination number of Mn^{2+}, making Mn(II) complexes sensitive to environment.[64] The structure regulation between four Mn(II) complexes in T_d and O_h ligand field expand potential applications for low-dimensional Mn(II) halide complexes.

The emission characteristics of Mn(II) halides are fundamentally governed by ligand field symmetry, where tetrahedral ($[MnX_4]^{2-}$) and octahedral ($[MnX_6]^{4-}$ or $[MnX_4L_2]^{2-}$) coordination geometries yield distinct green and red luminescence, respectively.[73, 91] Phase transitions between these configurations enable dynamic emission switching through three structural mechanisms, with optical responses quantifiable via crystal field parameters using Tanabe-Sugano diagrams (Figure 6a)[57, 73, 77]. This framework establishes that Racah parameters (B, C) describe electron-electron repulsion, while crystal field splitting (Δ) determines the $^4T_1(G)$ excited-state energy. Crucially, $\Delta O_h > \Delta T_d$ positions $^4T_1(G)$ (T_d) energetically above $^4T_1(G)$ (O_h), explaining the green-to-red emission shift is compositional systems like $[(CH_3)_4N]_2MnCl_4$ (green) and $(CH_3)_4NMnCl_3$ (red)[77] with Stokes shifts scaling proportionally to Δ magnitude (Figure 6b).

Structural transitions occur through: (1) Solvent mediation where molecules like ethanol in red-emitting $(C_4NOH_{10})_5Mn_2Cl_9 \cdot C_2H_5OH$ template $[Mn_2Cl_9]^{5-}$ connectivity without direct Mn^{2+} coordination, with thermal removal yielding green-emitting $[MnCl_4]^{2-}$ (Figure 7c,e)[61]. (2) Direct ligand coordination where H_2O converts $[MnX_4]^{2-}$ to distorted $[MnX_4(H_2O)_2]^{2-}$,[58, 64, 95] as demonstrated in hydration-driven transitions from red $CsMnBr_3:Pb^{2+}$ to green $Cs_3MnBr_5:Pb^{2+}$ nanocrystals (Figure 7d)[22]. While hydrated complexes typically exhibit red emission[58], centrosymmetry-induced Laporte forbiddance quenches luminescence, as evidenced by the PLQY reduction from 82% to 0% in hydrated $C_6N_2H_{16}MnBr_4$[64]. However, structural distortion enables anomalous blue emission[95] characterized by accelerated PL decay originates from sub-bandgap states facilitating non-radiative recombination pathways, and enhanced electron-phonon coupling mediated by O-H vibrational modes in coordinated H_2O molecules. Dehydration restores original luminescence, confirming reversibility[64].

These structure regulations enabled Mn(II) halides achieving predictable emission switching through well-defined structural mechanisms. Future research may: (1) Quantify relationships between lattice strain, ligand covalency, and distortion metrics to enable rational material design; (2) Explore distortion-engineered emission beyond conventional spectral ranges; (3) Optimize switching cyclability for robust anti-counterfeiting and optical encryption technologies leveraging environmental sensitivity[22, 64, 96].

3. Applications of Mn(Ⅱ) halide complexes

Lead halide perovskites has become a new class of promising materials in optoelectronic devices due to their excellent optoelectronic properties.[1, 2] Perovskites with the advantages of high luminescence performance, tunable emission and facile synthesis can achieve light-emitting diodes (LED) with high brightness, low cost, and wide color gamut for applications.[97-99] Along with the superior optoelectronic performance, the ability of form large, high-quality crystals and polycrystalline layers[100] making Lead halide perovskites one of the most promising materials for X-ray imaging technologies.[101] However, the toxicity and poor stability of lead perovskites have hindered their further applying.

To overcome the obstacle, a series of lead-free luminescent metal halide complexes have been developed, featuring diverse coordination geometries centered on Bi^{3+}, Sb^{3+}, Cu^+, Sn^{2+}, and Zr^{4+} ions coordinated with halide ligands..[102-110] Some lead-free metal halide complexes exhibit high luminescence performance with PLQY above 90%, such $(TEBA)_2SbCl_5$[106] as and $(C_9NH_{20})_2SbCl_5$[105], have been applied to white LEDs as phosphors. In addition to high PLQY, the large stokes shift make the lead-free metal halide complexes a promising material for radiation detection such as neutron[111] and X-ray imaging.[112-114] However, the lead-free metal halide based WLEDs can only be effectively pumped by UV light-emitting diode chip with lower efficiency than blue LED chip, leading to luminous efficacy loss of LED.[16] Mn(Ⅱ) halide complexes exhibit tunable green and red emission by crystal field and can be effectively pumped by blue chip, making it suitable for LED applications.

3.1. Light emitting diodes

3.1.1 Mn(Ⅱ) halide complexes as color conversion materials

According to the above description, Mn(Ⅱ) halide complexes achieve high PLQY in both green and red emissive region and can be excited by blue light (400-500 nm) through the $^6A_1$ to ^4G transition. The superior luminescent properties and thermal stability make Mn(Ⅱ) complexes promising material for blue chip pumped white LED (WLED) applications.

As for green 0D Mn(Ⅱ) halide complexes, the longer Mn-Mn distances in $[MnX_4]^{2-}$ lead to a high PLQY to near unity.[60, 66] Thus the four coordinated Mn(Ⅱ) complexes are applied as green phosphor in color conversion layer. A WLED can be fabricated by mixing the green emissive Mn(Ⅱ) phosphor and red-emitting $K_2SiF_6:Mn^{4+}$ (KSF) on blue chip[68, 87] as shown in Figure 8a. By mixing $(C_5H_6N)_2MnBr_4$ complexes with KSF, Deng et al. fabricated WLED with initial luminous efficacy of 93.90 lm W^{-1} on blue InGaN chip (460 nm). The corresponding WLED displayed zero-attenuation in emission intensity to 92.87 lm W^{-1} after continuous work after 410 minutes.[87] Xia et al. fabricated a WLED device by the $(C_{10}H_{16}N)_2MnBr_4$ and KSF phosphors on a blue InGaN chip (450 nm).[68] The WLED displayed correlated color temperature (CCT) of 7218 K and a high luminous efficacy up to 120 lm W^{-1} with the CIE chromaticity coordinates of (0.3054, 0.3088) located on the white region. The WLED covers a wide color gamut of 104% NTSC in CIE 1931 (Figure 8b). The green $(C_{10}H_{16}N)_2MnBr_4$ phosphor showed no temperature quenching behaviour below 150 °C (Figure 8c), which is attractive for use in the backlights of LCDs.

The other way to achieve LED from conversion layer with blue chip is by combining the green and red Mn(Ⅱ) halide complexes in one layer. Different from the lead halide perovskites that fast anion exchange take place within 5 minutes in one layer,[87] emissions of Mn(Ⅱ) halide complexes depends on T_d and O_h crystal field and are stable in on media with different compositions. Deng et al. fabricated LED devices through depositing the polystyrene (PS) film containing green emissive $(C_5H_6N)_2MnBr_4$ and red emissive $C_5H_6NMnCl_3$ phosphors on a blue chip.[87] The CRI and CCT can be further adjusted by changing the ratio between green and red Mn(Ⅱ) halide phosphors. Similarly, Ju et al. fabricated WLED based on conversion layer consist of $C_4H_{12}NMnCl_3$ and $(C_8H_{20}N)_2MnBr_4$.[16] The WLED performed outstanding luminous efficacy of 96 lm W^{-1} and a wide color gamut of 104% NTSC in CIE 1931 (Figure 8d and Figure 8e). The corresponding PL peak positions keep sTable 2nd photoluminescence intensity showed no obvious decrease after 3000 hours under continuous operation (Figure 8f).

3.1.2 Mn(Ⅱ) halide complexes as emitting materials

Besides of light conversion material, Mn(Ⅱ) halide complexes can also be used as light emitting materials in LEDs, which as electroluminescent LED (EL-LED) for distinguish.[17, 66] As shown in Figure 8g, Mn(Ⅱ) based EL-LED exhibit layer structure. Chen et al. applied $(Ph_4P)_2MnBr_4$ doped in host materials of TCTA and 26DCZPPY as emitting layer, achieving green EL-LED with turn-on voltage of 4.8 V and the peak luminance of 2339 cd m^{-2} with external quantum efficiency (EQE) of 9.6%.[66] Wang et al. fabricated red EL-LED with EL emission at 627 nm with CIE color coordinates (0.69, 0.31) through 0D $(ABI)_4MnBr_6$.[17] The corresponding red EL-LED exhibit the maximum recording brightness of 4700 cd m^{-2} and EQE of 9.8%, as shown in Figure 8h. The half-life of the device reaches 5.5 h at 5V (Figure 8i), which showed superior performance among the lead free red EL-LEDs.[115]

Owing to the luminescent properties and the stability, Mn(Ⅱ) halide complexes are promising lead-free materials for both WLEDs and monochrome EL-LEDs.

3.1.3 Mn(Ⅱ) halide complexes with circularly polarized luminescence

Beyond their conventional luminescence properties, manganese halides exhibit significant promise for applications in circularly polarized luminescence (CPL) materials.[116] CPL materials hold immense potential for advancing next-generation optoelectronic technologies, including circularly polarized light-emitting diodes (CP-LEDs)[65], three-dimensional (3D) displays, CPL switches, and CPL detectors[117, 118]. Manganese-based halides are particularly attractive candidates for high-performance CPL materials due to their exceptional photochemical stability, high photoluminescence quantum yields (PLQY), low toxicity, and potential for incorporating additional functionalities such as ferroelectricity and magneto-chiroptical coupling.

Recent research has actively explored manganese halides as CPL emitters. Chen *et al.* synthesized chiral complexes (D)- and (L)-(tert-butyl prolinate)MnCl₃, achieving dissymmetry factors g of

ARTICLE

6.1 × 10^{-3} and -6.3 × 10^{-3}, respectively[86]. Subsequently, Artem'ev *et al.* reported R/S-[MBA-Me₃]MnBr₄ with g of 4.5*10^{-3} [65]. Chen *et al.* further demonstrated significantly enhanced performance in R/S-DACAMnBr₃ [119], achieving larger g values of 0.292 and 0.231. Notably, many CPL-active manganese halides, including 0D green emitters, exhibit one-dimensional long-range order in crystal structures[67, 120-122]. This structural predisposition appears favorable for CPL generation. Given that red-emitting manganese halides also frequently adopt 1D structural motifs (Table 2), they demonstrate considerable potential for future CPL material development. Manganese halides emerge as highly promising platforms for circularly polarized luminescence, leveraging their inherent material advantages and structural versatility. The observed propensity for 1D crystal structures, common in both green- and red-emitting variants, coupled with recent demonstrations of significant dissymmetry factors, underscores their strong potential for realizing efficient and functional CPL materials.

3.2. Radiation Detection

3.2.1 Neutron imaging

Due to large Stokes shift and high PLQY, Mn-doped perovskite NCs have huge potential to fast neutron Imaging. Fast neutrons are uncharged elementary particles with kinetic elementary energy exceeding 1 MeV, which have low interaction cross sections and high penetration depths for both high- and low-Z elements. As a contrast, other types of radiation sources, such as X- rays, γ-rays, and thermal neutrons only respond to heavy or light elements. Therefore, fast neutrons imaging is increasingly a nondestructive detection technology for large-scale samples of dense, mixed-Z compositions. However, the resolution of fast neutron imaging is still limited by conventional scintillator materials. In 2020, McCall et al first reported recoil proton detector based on colloidal semiconductor NCs in solvents with high hydrogen-density.[111] It is noteworthy that Mn-doped CsPbClBr₂ perovskite NCs offer the best spatial resolution with 27 pixels because of the highest Stokes shift among a variety of semiconductor NCs tested. Subsequent, the same research group synthesized the ultra-high load concentrations (>100 mg mL⁻¹) Mn-doped CsPbClBr₂ NCs through using 3-(N, N-dimethyloctadecylammonio) propane sulfonate (ACS18) as the zwitterionic ligand, promoting 8 times brighter light yield than oleyl-capped NCs under fast neutron irradiation.[43] Although Mn-doped CsPbClBr₂ NCs as fast neutron scintillator have exhibited improved resolution and light yield, the liquid suspension is inconvenient to use for realistic imaging purposes. Another feasible strategy is that Zheng et al. proposed a single-component 2D Mn-doped (C₁₈H₃₇NH₃)₂PbBr₄ perovskite scintillator, in which hydrogen-rich organic components absorb fast neutron and Mn²⁺ dopants acts as luminescence centers in the perovskite that could offer high Stokes shift and avoid self-absorption.[18] Mn-doped (C₁₈H₃₇NH₃)₂PbBr₄ scintillator was finally made into imaging plates for fast neutron radiography with 0.5 lp mm⁻¹ spatial resolution, but its light yield still falls behind commercial ZnS (Ag): PP scintillator screen. In the future, effective methods

should be explored to enhance the interaction between Mn doped perovskite and fast neutrons and improve its light yield.

3.2.2 X-ray imaging

As for X-ray imaging, a large Stokes shift is essential in order to avoid self-absorption within the relatively thick scintillating layer.[101] Mn(Ⅱ) complexes exhibit large stokes shift between $^6A_1(S)$ to $^4T_1(G)$ excitation and corresponding $^4T_1(G)$ to $^6A_1(S)$ emission, indicating less degree of self-absorption under X-ray excitation. The superior luminescent properties and large stokes shift make Mn(Ⅱ) complexes as efficient X-ray scintillators for X-ray imaging.

As a group of low toxic candidate for X-ray scintillators, many Mn(Ⅱ) complexes exhibit superior steady-state X-ray light yields than commercial BGO (10000 photons MeV⁻¹), CsI:Tl (54000 photons MeV⁻¹), CsI:Na (41000 photons MeV⁻¹), LuAG:Ce (22000 photons MeV⁻¹) and toxic CsPbBr₃ (21000 photons MeV⁻¹)[123] as displayed in Figure 9.[16, 19, 65, 69, 83, 94, 124] Among them, the green emissive (C₃₈H₃₄P₂)MnBr₄[19], TPP₂MnBr₄[125], (Br-BzTPP)₂MnBr₄[71] and red emissive C₄H₁₂NMnCl₃[16] Mn(Ⅱ) complex X-ray scintillations have reached high light yield of 80 000 photons MeV⁻¹, 78 000±2000 photons MeV⁻¹, 80 100 photons MeV⁻¹ and 50 500 photons MeV⁻¹, respectively.

Another important parameter for scintillators is the evaluation of afterglow. A high afterglow can reduce the signal-to-noise ratio of the X-ray imaging. Thus, it is always desirable to reduce the afterglow to obtain X-ray imaging with high contrast especially for CT imaging. Compared with the commercial CsI:Tl (1.5% @3 ms), the Mn(Ⅱ) complex X-ray scintillations exhibit lower residual afterglow signal as shown in Table 3.

The detection limit of X-ray dose rate required for X-ray medical diagnostics is 5.5 μGy S⁻¹.[126] For Mn(Ⅱ) complex X-ray scintillations, the detection limit can reach as low as 8.8 nGy s⁻¹,[125] which is about 625 times lower than the requirement. A high spatial resolution of 15.7 lp mm⁻¹ was achieved in TPP₂MnBr₄ X-ray scintillation imaging, superior than the Eu³⁺ doped CsPbBr₃ glass-ceramic (10 000 photons MeV⁻¹, 15.0 lp mm⁻¹) [127] and performing higher light yield (Table 3). Furthermore, the Mn(Ⅱ) complex can be imbedded in to flexible matrix such as PDMS to build a flexible scintillator remaining good resolution, expanding the corresponding application.[19]

Manganese(II) halide complexes have emerged as promising lead-free alternatives in optoelectronics, addressing the toxicity and stability limitations of lead halide perovskites despite their superior photophysical properties. While diverse lead-free metal halide (e.g., based on Bi³⁺, Sb³⁺, Cu⁺ exhibit high PLQY and potential in radiation detection, their reliance on UV excitation limits white light-emitting diode (WLED) efficiency. Mn(II) halides overcome this constraint through blue-light-excitable green/red emission tunable via crystal field engineering. For WLEDs, tetrahedral [MnX₄]²⁻ complexes achieve near-unity PLQY and serve as efficient color converters when blended with red phosphors on blue chips, delivering high luminous efficacy and thermal stability up to 150°C. Alternatively, hybrid green/red Mn(II) phosphor layers in polymer matrices enable stable, tunable WLEDs with negligible efficiency decreasing after 3000 hours. Beyond photoluminescence, Mn(II)

complexes function as electroluminescent emitters in LEDs, achieving green emission and red luminescence.

In radiation detection, large Stokes shift of Mn halides minimizes self-absorption, enabling efficient X-ray scintillators with light yields (50,500–80,100 photons MeV^{-1} exceeding commercial scintillators, ultralow detection limits and high spatial resolution (Table 3). For neutron imaging, Mn-doped $CsPbClBr_2$ provide high spatial resolution via recoil proton detection[43], while 2D Mn-doped lead halides offers solid-state alternatives despite lower light yield[18]. Furthermore, chiral Mn(II) halides demonstrate significant circularly polarized luminescence (CPL) with dissymmetry factors up to 0.292 [81, 127], attributed to their prevalent 1D structures and enabling applications in CP-LEDs, 3D displays, and optical switches.

Therefore, Mn(II) halides constitute a versatile, environmentally benign platform for advanced optoelectronics, excelling in blue-pumped WLEDs, high-resolution radiation detection, and chiroptical devices. This multifunctionality stems directly from their tunable emission, exceptional stability, and structurally adaptive coordination chemistry, positioning them as a cornerstone for sustainable photonic materials innovation.

4. Conclusions and outlooks

In this perspective, we have summarized the recent progress on Mn(II) complexes through their structure and luminescent properties. The properties of color tunable, high PLQY, large stokes shift and thermal stability make Mn(II) complexes a class of promising materials on LED and Radiation Detection such as neutron and X-ray imaging.

Luminescent properties are mainly determined by the environment of centre Mn^{2+}. Dopant Mn^{2+} exhibit orange emission in lead halide perovskite host. The luminescent performances depend on the bandgap of the perovskite host and Mn^{2+} ions doping concentration. As for green emissive Mn(II) halide phosphors, the emission and excitation are affected by four-fold coordinated $[MnX_4]^{2-}$ tetrahedron in 0D structure. The PLQY of Mn(II) halides is primarily governed by Mn-Mn interatomic distances, the Stokes shift is modulated by angular distortion within the crystal structure and FWHM is determined by electron-phonon coupling influenced by structural distortions and organic A-site cations[23, 26, 81, 82]. The red emission of Mn(II) complexes is derived from $[MnX_6]^{4-}$ octahedrons through six-fold coordinated $[MnX_6]^{4-}$ octahedrons. The $[MnX_6]^{4-}$ octahedron units can connect through face-sharing and further crystalize to 0D and 1D structure. However, d-d transition of Mn^{2+} in the centrosymmetric octahedral crystal field is forbidden, leading to a low PLQY for red emissive Mn(II) complexes. Thus, distortion of $[MnX_6]^{4-}$ octahedrons from both Mn-X length and X-Mn-X angle in structure are necessary to achieve superior luminescence performance. Green emissive Mn(II) complexes with PLQY to near unity and red emissive Mn(II) complexes with PLQY over 90% have already been achieved in previous researches.

The performance in luminescent property, stability and low toxic nature makes Mn(II) complexes suitable for LED and X-ray imaging applications. Mn(II) complexes are applied as color conversion materials on blue chip. The luminous efficacy of LED based on Mn(II) complex and KSF phosphors reached up to 120 lm/W. The luminous efficacy of LED fabricated by Mn(II) complexes as both green and red phosphors reached up 96 lm/W. Besides, Mn(II) complexes can also be used as emitting material in EL-LED. Red EL-LED with the maximum recording brightness of 4700 cd m^{-2} and EQE of 9.8% was achieved by $(ABI)_4MnBr_6$, which showed superior performance among the lead free red EL-LEDs. Manganese halides also exhibit promise for applications in CPL materials,[116] which hold immense potential for advancing next-generation optoelectronic technologies, including circularly polarized light-emitting diodes (CP-LEDs)[65], three-dimensional (3D) displays, CPL switches, and CPL detectors[117, 118]. Because of large stokes shift, Mn(II) complexes are thought promising materials on efficient radiation detection such as neutron and X-ray imaging. The spatial resolution for neutron scintillators reached 27 pixels by Mn-doped $CsPbClBr_2$ perovskite NCs. The currently prepared Mn(II) complex X-ray scintillators displayed a highest Light yield to 80 000 photons MeV^{-1}, spatial resolution of 25 lp mm^{-1} and lowest detection limit of 8.8 nGy s^{-1}.

Although these results are encouraging, there still exist further improvement in Mn(II) complexes for both theoretical research and practical applications. (i) Material balancing efficiency and stability: the future development of Mn-based halides hinges on resolving the inherent trade-off between PLQY and thermal and environmental stability. For both tetrahedrally coordinated green emitters and octahedrally coordinated red emitters, achieving high PLQY requires sufficient Mn-Mn separation distances. Small inorganic cations may therefore not be suitable due to their tendency to decreasing Mn-Mn distance. Two strategies can address this challenge: Mn doping within octahedral/tetrahedral host frameworks[25] or incorporation of bulky rigid organic A-site cations[81], enabling adequate Mn-Mn spacing while simultaneously enhancing material stability. (ii) Theoretical quantifying structure-property relationships: recently Zhu et al.[85] has quantitatively correlated Mn octahedral distance mismatch with red emission efficiency in Mn-based halides. However, a quantitative or semi-quantitative understanding of how lattice distortions in high-symmetry octahedra govern excitonic behavior remains critical. For octahedrally coordinated red emitters, establishing correlations between crystallographic parameters (e.g., bond length mismatch[85] and bond angle distortion[128]) and PLQY will provide essential guidelines for designing efficient Mn-halide phosphors. Machine learning models that map crystallographic descriptors to optical outputs could further accelerate the discovery of high-performance red-emitting Mn halides. (iii) Application-driven innovations: colloidal Mn-based nanocrystals with narrow emission linewidths are essential for red and green color conversion layers in next-generation micro-LEDs[129]. A key advantage of Mn halides lies in their compatibility with high-temperature hot-injection methods, similar with lead halide perovskites, for synthesizing small-sized colloidal NCs. Advancing pixel-level patterning techniques for these nanomaterials could enable environmentally friendly color-

conversion micro-LED technologies. Furthermore, Mn（Ⅱ） halides have high halogen content, showing promising prospects as scintillators. Developing highly luminescent Mn bromides/iodides with elevated atomic numbers (Z) may enable efficient X-ray scintillators through enhanced photon attenuation and radiative recombination.

Manganese halides constitute a versatile, lead-free platform with tunable emission, large Stokes shifts, and exceptional stability. Future progress hinges on elucidating structure-distortion-property relationships, advancing synthetic control for environmental resilience, and pioneering device paradigms that leverage their unique photo-physics. Cross-disciplinary efforts integrating crystallography, spectroscopy, and device engineering will accelerate their deployment in next-generation optoelectronics and radiation detection.

Author Contributions

The manuscript was written through contributions of all authors. All authors have given approval to the final version of the manuscript.

Conflicts of interest

There are no conflicts to declare.

Acknowledgements

Notes and references

1. A. K. Jena, A. Kulkarni and T. Miyasaka, Halide Perovskite Photovoltaics: Background, Status, and Future Prospects, *Chemical Reviews*, 2019, **119**, 3036-3103.

2. J. Shamsi, A. S. Urban, M. Imran, L. De Trizio and L. Manna, Metal Halide Perovskite Nanocrystals: Synthesis, Post-Synthesis Modifications, and Their Optical Properties, *Chemical Reviews*, 2019, **119**, 3296-3348.

3. J. Li, H.-L. Cao, W.-B. Jiao, Q. Wang, M. Wei, I. Cantone, J. Lü and A. Abate, Biological impact of lead from halide perovskites reveals the risk of introducing a safe threshold, *Nature Communications*, 2020, **11**, 310.

4. Y. Li, Z. Shi, W. Liang, J. Ma, X. Chen, D. Wu, Y. Tian, X. Li, C. Shan and X. Fang, Recent advances toward environment-friendly photodetectors based on lead-free metal halide perovskites and perovskite derivatives, *Materials Horizons*, 2021, **8**, 1367-1389.

5. I. Infante and L. Manna, Are There Good Alternatives to Lead Halide Perovskite Nanocrystals?, *Nano Letters*, 2021, **21**, 6-9.

6. A. Swarnkar, V. K. Ravi and A. Nag, Beyond Colloidal Cesium Lead Halide Perovskite Nanocrystals: Analogous Metal Halides and Doping, *ACS Energy Letters*, 2017, **2**, 1089-1098.

7. R. N. Bhargava, D. Gallagher, X. Hong and A. Nurmikko, Optical properties of manganese-doped nanocrystals of ZnS, *Physical Review Letters*, 1994, **72**, 416-419.

8. V. Proshchenko and Y. Dahnovsky, Tunable Luminescence in CdSe Quantum Dots Doped by Mn Impurities, *The Journal of Physical Chemistry C*, 2014, **118**, 28314-28321.

9. J. H. Yu, S.-H. Kwon, Z. Petrášek, O. K. Park, S. W. Jun, K. Shin, M. Choi, Y. I. Park, K. Park, H. B. Na, N. Lee, D. W. Lee, J. H. Kim, P. Schwille and T. Hyeon, High-resolution three-photon biomedical imaging using doped ZnS nanocrystals, *Nature Materials*, 2013, **12**, 359-366.

10. D.-Y. Jo, D. Kim, J.-H. Kim, H. Chae, H. J. Seo, Y. R. Do and H. Yang, Tunable White Fluorescent Copper Gallium Sulfide Quantum Dots Enabled by Mn Doping, *ACS Applied Materials & Interfaces*, 2016, **8**, 12291-12297.

11. P. K. Santra and P. V. Kamat, Mn-Doped Quantum Dot Sensitized Solar Cells: A Strategy to Boost Efficiency over 5%, *J. Am. Chem. Soc.*, 2012, **134**, 2508-2511.

12. F. Carulli, F. Cova, L. Gironi, F. Meinardi, A. Vedda and S. Brovelli, Stokes Shift Engineered Mn:CdZnS/ZnS Nanocrystals as Reabsorption-Free Nanoscintillators in High Loading Polymer Composites, *Advanced Optical Materials*, 2022, **10**, 2200419.

13. C. S. Erickson, L. R. Bradshaw, S. McDowall, J. D. Gilbertson, D. R. Gamelin and D. L. Patrick, Zero-Reabsorption Doped-Nanocrystal Luminescent Solar Concentrators, *ACS Nano*, 2014, **8**, 3461-3467.

14. D. Parobek, B. J. Roman, Y. Dong, H. Jin, E. Lee, M. Sheldon and D. H. Son, Exciton-to-Dopant Energy Transfer in Mn-Doped Cesium Lead Halide Perovskite Nanocrystals, *Nano Letters*, 2016, **16**, 7376-7380.

15. W. Liu, Q. Lin, H. Li, K. Wu, I. Robel, J. M. Pietryga and V. I. Klimov, Mn2+-Doped Lead Halide Perovskite Nanocrystals with Dual-Color Emission Controlled by Halide Content, *Journal of the American Chemical Society*, 2016, **138**, 14954-14961.

16. T. Jiang, W. Ma, H. Zhang, Y. Tian, G. Lin, W. Xiao, X. Yu, J. Qiu, X. Xu, Y. Yang and D. Ju, Highly Efficient and Tunable Emission of Lead-Free Manganese Halides toward White Light-Emitting Diode and X-Ray Scintillation Applications, *Advanced Functional Materials*, 2021, **31**, 2009973.

17. S. Yan, W. Tian, H. Chen, K. Tang, T. Lin, G. Zhong, L. Qiu, X. Pan and W. Wang, Synthesis of 0D Manganese-Based Organic–Inorganic Hybrid Perovskite and Its Application in Lead-Free Red Light-Emitting Diode, *Advanced Functional Materials*, 2021, **31**, 2100855.

18. J. Zheng, Y. Zeng, J. Wang, C. Sun, C. Tang, Y. Wu, Y. Zhang, Y. Yi, N. Wang, Y. Zhao and S. Zhou, Hydrogen-Rich 2D Halide Perovskite Scintillators for Fast Neutron Radiography, *J. Am. Chem. Soc.*, 2021, DOI: 10.1021/jacs.1c08923.

19. L.-J. Xu, X. Lin, Q. He, M. Worku and B. Ma, Highly efficient eco-friendly X-ray scintillators based on an organic manganese halide, *Nature Communications*, 2020, **11**, 4329.

20. Q. Zhou, L. Dolgov, A. M. Srivastava, L. Zhou, Z. Wang, J. Shi, M. D. Dramićanin, M. G. Brik and M. Wu, Mn2+ and Mn4+ red phosphors: synthesis, luminescence and applications in WLEDs. A review, *Journal of Materials Chemistry C*, 2018, **6**, 2652-2671.

21. F. Yu, H.-R. Zhang, W.-W. Gao, C.-Y. Fang, Y.-N. Chen, M.-L. Xu, X.-W. Lei, X.-W. Kong and C.-Y. Yue, One-Dimensional Red Light–Emissive Organic Manganese(II) Halides as X-Ray Scintillators, *Inorganic Chemistry*, 2024, **63**, 18146-18153.

22. J. Ren, L. Liu, H. Liu, X. Zhou, J. Li, F. Liu, L. Chen, G. Yan and Y. Wang, Lead-Doped Cesium Manganese Halide Perovskite Nanocrystals for Light-Emitting Diodes: Room-Temperature Synthesis, Energy Transfer, and Phase Modulating, *ACS Materials Letters*, 2025, **7**, 1028-1034.

23. D. D. Wang, H. M. Dong, L. L. Zhang, D. Wu, L. Y. Ren, D. X. Zhao, T. Wang and M. Feng, Yellow-Emitting Organic-Inorganic Hybrid Manganese Halides Realized by Br/Cl Composition Engineering, *Laser & Photonics Reviews*, 2025, **n/a**, 2401982.

24. J. Hou, R. Liu, P. Han, C. Luo, Z. Ding, W. Zhou, C. Li, J. Li, Y. Zhao, J. Chen, J. Liu and B. Yang, Unveiling the Localized Exciton-Based Photoluminescence of Manganese Doped Cesium Zinc Halide Nanocrystals, *Nano Letters*, 2023, **23**, 3762-3768.

25. Y. Yang, B. Ke, C. Yang, Y. Xue, K. Huang, X. Lu and B. Zou, Multifunctional applications enabled by tunable multi-emission and ultra-broadband VIS-NIR luminescence via energy transfer in Sn^{2+}/Mn^{2+}-doped lead-free Zn-based metal halides, *Materials Horizons*, 2025, DOI: 10.1039/d4mh01821d.

26. B. He, B. Ke, C. Yang, Y. Chen, X. Zhong, W. Li and B. Zou, Efficient and Stable Red-Orange Emission from Polaronic Magnetic Excitons in Mn (II)-Doped 0D All-Inorganic Rb_4CdCl_6, *Advanced Optical Materials*, 2025, **13**, 2402624.

27. J. Ghosh, M. Hossain and P. K. Giri, Origin and tunability of dual color emission in highly stable Mn doped $CsPbCl_3$ nanocrystals grown by a solid-state process, *Journal of Colloid and Interface Science*, 2020, **564**, 357-370.

28. S. Oh, S. W. Bae, T. H. Kim, G. Kang, H. Jung, Y.-H. Kim and M. Park, Highly transparent all-perovskite luminescent solar concentrator/photovoltaic windows, *Journal of Materials Chemistry A*, 2024, **12**, 33193-33202.

29. X. Feng, Y. Sheng, K. Ma, F. Xing, C. Liu, X. Yang, H. Qian, S. Zhang, Y. Di, Y. Liu and Z. Gan, Multi-Level Anti-Counterfeiting and Optical Information Storage Based on Luminescence of Mn-Doped Perovskite Quantum Dots, *Advanced Optical Materials*, 2022, **10**, 2200706.

30. N. Pradhan, Red‐Tuned Mn d–d Emission in Doped Semiconductor Nanocrystals, *ChemPhysChem*, 2016, **17**, 1087-1094.

31. D. Parobek, Y. Dong, T. Qiao and D. H. Son, Direct Hot-Injection Synthesis of Mn-Doped $CsPbBr_3$ Nanocrystals, *Chemistry of Materials*, 2018, **30**, 2939-2944.

32. Q. A. Akkerman, D. Meggiolaro, Z. Dang, F. De Angelis and L. Manna, Fluorescent Alloy $CsPb_xMn_{1–x}I_3$ Perovskite Nanocrystals with High Structural and Optical Stability, *ACS Energy Letters*, 2017, **2**, 2183-2186.

33. C.-W. Wang, X. Liu, T. Qiao, M. Khurana, A. V. Akimov and D. H. Son, Photoemission of the Upconverted Hot Electrons in Mn-Doped $CsPbBr_3$ Nanocrystals, *Nano Letters*, 2022, **22**, 6753-6759.

34. C. Orrison, J. R. Meeder, B. Zhang, J. Puthenpurayil, M. B. Hall, M. Nippe and D. H. Son, Efficient Redox-Neutral Photocatalytic Formate to Carbon Monoxide Conversion Enabled by Long-Range Hot Electron Transfer from Mn-Doped Quantum Dots, *J. Am. Chem. Soc.*, 2021, **143**, 10292-10300.

35. H. Liu, Z. Wu, J. Shao, D. Yao, H. Gao, Y. Liu, W. Yu, H. Zhang and B. Yang, $CsPb_xMn_{1–x}Cl_3$ Perovskite Quantum Dots with High Mn Substitution Ratio, *ACS Nano*, 2017, **11**, 2239-2247.

36. W. Q. Peng, S. C. Qu, G. W. Cong and Z. G. Wang, Concentration effect of Mn^{2+} on the photoluminescence of ZnS:Mn nanocrystals, *Journal of Crystal Growth*, 2005, **279**, 454-460.

37. X. Yang, C. Pu, H. Qin, S. Liu, Z. Xu and X. Peng, Temperature- and Mn^{2+} Concentration-Dependent Emission Properties of Mn^{2+}-Doped ZnSe Nanocrystals, *J. Am. Chem. Soc.*, 2019, **141**, 2288-2298.

38. S. Das Adhikari, A. Dutta, S. K. Dutta and N. Pradhan, Layered Perovskites $L_2(Pb_{1–x}Mn_x)Cl_4$ to Mn-Doped $CsPbCl_3$ Perovskite Platelets, *ACS Energy Letters*, 2018, **3**, 1247-1253.

39. A. S. Silva, S. A. Lourenço and N. O. Dantas, Mn concentration-dependent tuning of Mn^{2+} d emission of $Zn_{1–x}Mn_xTe$ nanocrystals grown in a glass system, *Physical Chemistry Chemical Physics*, 2016, **18**, 6069-6076.

40. A. De, N. Mondal and A. Samanta, Luminescence tuning and exciton dynamics of Mn-doped $CsPbCl_3$ nanocrystals, *Nanoscale*, 2017, **9**, 16722-16727.

41. V. Naresh, M.-K. Cho, P.-R. Cha and N. Lee, Polar-Solvent-Free Sonochemical Synthesis of Mn(II)-Doped $CsPbCl_3$ Perovskite Nanocrystals for Dual-Color Emission, *ACS Applied Nano Materials*, 2023, **6**, 4693-4706.

42. S. Zou, Y. Liu, J. Li, C. Liu, R. Feng, F. Jiang, Y. Li, J. Song, H. Zeng, M. Hong and X. Chen, Stabilizing Cesium Lead Halide Perovskite Lattice through Mn(II) Substitution for Air-Stable Light-Emitting Diodes, *J. Am. Chem. Soc.*, 2017, **139**, 11443-11450.

43. F. Montanarella, K. M. Mccall, K. Sakhatskyi, S. Yakunin, P. Trtik, C. Bernasconi, I. Cherniukh, D. Mannes, M. I. Bodnarchuk, M. Strobl, B. Walfort and M. V. Kovalenko, Highly Concentrated, Zwitterionic Ligand-Capped Mn^{2+}:$CsPb(Br_xCl_{1–x})_3$ Nanocrystals as Bright Scintillators for Fast Neutron Imaging, *ACS Energy Letters*, 2021, DOI: 10.1021/acsenergylett.1c01923, 4365-4373.

44. S. Paul, E. Bladt, A. F. Richter, M. Döblinger, Y. Tong, H. Huang, A. Dey, S. Bals, T. Debnath, L. Polavarapu and J. Feldmann, Manganese‐Doping‐Induced Quantum Confinement within Host Perovskite Nanocrystals through Ruddlesden‐Popper Defects, *Angewandte Chemie International Edition*, 2020, **59**, 6794-6799.

45. J. Zhu, X. Yang, Y. Zhu, Y. Wang, J. Cai, J. Shen, L. Sun and C. Li, Room-Temperature Synthesis of Mn-Doped Cesium Lead Halide Quantum Dots with High Mn Substitution Ratio, *J Phys Chem Lett*, 2017, **8**, 4167-4171.

46. L. Protesescu, S. Yakunin, M. I. Bodnarchuk, F. Krieg, R. Caputo, C. H. Hendon, R. X. Yang, A. Walsh and M. V. Kovalenko, Nanocrystals of Cesium Lead Halide Perovskites ($CsPbX_3$, X = Cl, Br, and I): Novel Optoelectronic Materials Showing Bright Emission with Wide Color Gamut, *Nano Lett*, 2015, **15**, 3692-3696.

47. M. Imran, V. Caligiuri, M. Wang, L. Goldoni, M. Prato, R. Krahne, L. De Trizio and L. Manna, Benzoyl Halides as Alternative Precursors for the Colloidal Synthesis of Lead-Based Halide Perovskite Nanocrystals, *J. Am. Chem. Soc.*, 2018, **140**, 2656-2664.

48. S. Das Adhikari, S. K. Dutta, A. Dutta, A. K. Guria and N. Pradhan, Chemically Tailoring the Dopant Emission in Manganese-Doped $CsPbCl_3$ Perovskite Nanocrystals, *Angewandte Chemie*, 2017, **129**, 8872-8876.

49. S. Zhou, S. Zhu, Y. Zhong, F. Tian, H. Huang, J. Chen and D. Chen, Chlorine-additive-promoted incorporation of Mn^{2+}

dopants into CsPbCl3 perovskite nanocrystals, *Nanoscale*, 2019, **11**, 12465-12470.

50. S. Das Adhikari, R. K. Behera, S. Bera and N. Pradhan, Presence of Metal Chloride for Minimizing the Halide Deficiency and Maximizing the Doping Efficiency in Mn(II)-Doped CsPbCl3 Nanocrystals, *The Journal of Physical Chemistry Letters*, 2019, **10**, 1530-1536.

51. A. Dutta, R. K. Behera, P. Pal, S. Baitalik and N. Pradhan, Near-Unity Photoluminescence Quantum Efficiency for All CsPbX3 (X=Cl, Br, and I) Perovskite Nanocrystals: A Generic Synthesis Approach, *Angew Chem Int Ed Engl*, 2019, **58**, 5552-5556.

52. Y. Li, C. Wang, G. Hu, W. Meng, S. Sui and Z. Deng, Promoting the doping efficiency and photoluminescence quantum yield of Mn-doped perovskite nanocrystals via two-step hot-injection, *Chem Commun (Camb)*, 2022, **58**, 941-944.

53. Z. Deng, L. Tong, M. Flores, S. Lin, J.-X. Cheng, H. Yan and Y. Liu, High-Quality Manganese-Doped Zinc Sulfide Quantum Rods with Tunable Dual-Color and Multiphoton Emissions, *Journal of the American Chemical Society*, 2011, **133**, 5389-5396.

54. Y. Li, S. Qi, P. Li and Z. Wang, Research progress of Mn doped phosphors, *RSC Advances*, 2017, **7**, 38318-38334.

55. E. H. Song, Y. Y. Zhou, Y. Wei, X. X. Han, Z. R. Tao, R. L. Qiu, Z. G. Xia and Q. Y. Zhang, A thermally stable narrow-band green-emitting phosphor MgAl2O4:Mn2+ for wide color gamut backlight display application, *Journal of Materials Chemistry C*, 2019, **7**, 8192-8198.

56. Y. Zhu, Y. Liang, S. Liu, H. Li and J. Chen, Narrow-Band Green-Emitting Sr2MgAl22O36:Mn2+ Phosphors with Superior Thermal Stability and Wide Color Gamut for Backlighting Display Applications, *Advanced Optical Materials*, 2019, **7**, 1801419.

57. V. Morad, I. Cherniukh, L. Pöttschacher, Y. Shynkarenko, S. Yakunin and M. V. Kovalenko, Manganese(II) in Tetrahedral Halide Environment: Factors Governing Bright Green Luminescence, *Chemistry of Materials*, 2019, **31**, 10161-10169.

58. H. Xiao, P. Dang, X. Yun, G. Li, Y. Wei, Y. Wei, X. Xiao, Y. Zhao, M. S. Molokeev, Z. Cheng and J. Lin, Solvatochromic Photoluminescent Effects in All-Inorganic Manganese(II)-Based Perovskites by Highly Selective Solvent-Induced Crystal-to-Crystal Phase Transformations, *Angewandte Chemie International Edition*, 2021, **60**, 3699-3707.

59. C. Jiang, N. Zhong, C. Luo, H. Lin, Y. Zhang, H. Peng and C.-G. Duan, (Diisopropylammonium)2MnBr4: a multifunctional ferroelectric with efficient green-emission and excellent gas sensing properties, *Chemical Communications*, 2017, **53**, 5954-5957.

60. M. Li, J. Zhou, M. S. Molokeev, X. Jiang, Z. Lin, J. Zhao and Z. Xia, Lead-Free Hybrid Metal Halides with a Green-Emissive [MnBr4] Unit as a Selective Turn-On Fluorescent Sensor for Acetone, *Inorganic Chemistry*, 2019, **58**, 13464-13470.

61. M.-E. Sun, Y. Li, X.-Y. Dong and S.-Q. Zang, Thermoinduced structural-transformation and thermochromic luminescence in organic manganese chloride crystals, *Chemical Science*, 2019, **10**, 3836-3839.

62. L. Mao, P. Guo, S. Wang, A. K. Cheetham and R. Seshadri, Design Principles for Enhancing Photoluminescence Quantum Yield in Hybrid Manganese Bromides, *Journal of the American Chemical Society*, 2020, **142**, 13582-13589.

63. H.-M. Pan, Q.-L. Yang, X.-X. Xing, J.-P. Li, F.-L. Meng, X. Zhang, P.-C. Xiao, C.-Y. Yue and X.-W. Lei, Enhancement of the photoluminescence efficiency of hybrid manganese halides through rational structural design, *Chemical Communications*, 2021, **57**, 6907-6910.

64. H.-L. Liu, H.-Y. Ru, M.-E. Sun, Z.-Y. Wang and S.-Q. Zang, Organic–Inorganic Manganese Bromide Hybrids with Water-Triggered Luminescence for Rewritable Paper, *Advanced Optical Materials*, 2022, **10**, 2101700.

65. M. P. Davydova, L. Q. Meng, M. I. Rakhmanova, I. Y. Bagryanskaya, V. S. Sulyaeva, H. Meng and A. V. Artem'ev, Highly Emissive Chiral Mn(II) Bromide Hybrids for UV-Pumped Circularly Polarized LEDs and Scintillator Image Applications, *Advanced Optical Materials*, 2023, **11**, 2202811.

66. L.-J. Xu, C.-Z. Sun, C. Xiao, Y. Wu and Z.-N. Chen, Green-Light-Emitting Diodes based on Tetrabromide Manganese(II) Complex through Solution Process, *Advanced Materials*, 2017, **29**, 1605739.

67. P. Tao, S.-J. Liu and W.-Y. Wong, Phosphorescent Manganese(II) Complexes and Their Emerging Applications, *Advanced Optical Materials*, 2020, **8**, 2000985.

68. G. Zhou, Z. Liu, J. Huang, M. S. Molokeev, Z. Xiao, C. Ma and Z. Xia, Unraveling the Near-Unity Narrow-Band Green Emission in Zero-Dimensional Mn2+-Based Metal Halides: A Case Study of (C10H16N)2Zn1–xMnxBr4 Solid Solutions, *The Journal of Physical Chemistry Letters*, 2020, **11**, 5956-5962.

69. T. Xu, W. Li, Z. Zhou, Y. Li, M. Nikl, M. Buryi, J. Zhu, G. Niu, J. Tang, G. Ren and Y. Wu, 0D Organic Manganese(II) Bromide Hybrids as Stable and Efficient X-Ray Scintillator, *physica status solidi (RRL) – Rapid Research Letters*, 2022, **16**, 2200175.

70. H. Dong, Y. Sun, L. Zhang, D. Wu, H. Shen, G. Pan, H. Wu, H. Wu, Z. Hao and J. Zhang, Near-Unity Narrow Green Emitting in Manganese Halides Realized by Direct Precipitation Synthesis, *Laser & Photonics Reviews*, 2025, **19**, 2400365.

71. Z. Gong, J. Zhang, X. Deng, M.-P. Ren, W.-Q. Wang, Y.-J. Wang, H. Cao, L. Wang, Y.-C. He and X.-W. Lei, Near-unity broadband emissive hybrid manganese bromides as highly-efficient radiation scintillators, *Aggregate*, 2024, **5**, e574.

72. S. Chen, C. Guo, S.-C. Chen, Y. Di, X. Fang, M.-J. Lin and H. Yang, Enhanced Stability of Melt-Processable Organic–Inorganic Hybrid Manganese Halides for X-Ray Imaging, *Small*, 2024, **20**, 2406032.

73. Y. Rodríguez-Lazcano, L. Nataf and F. Rodríguez, Pressure-induced transformation from isolated MnX4(Td) to exchange-coupled MnX6(Oh) in A2MnX4 (X: Cl, Br) crystals. Structural correlations by time-resolved spectroscopy, *Journal of Luminescence*, 2009, **129**, 2000-2003.

74. B. Su, M. S. Molokeev and Z. Xia, Mn2+-Based narrow-band green-emitting Cs3MnBr5 phosphor and the performance optimization by Zn2+ alloying, *Journal of Materials Chemistry C*, 2019, **7**, 11220-11226.

75. A. Jana, S. Zhumagali, Q. Ba, A. S. Nissimagoudar and K. S. Kim, Direct emission from quartet excited states triggered by upconversion phenomena in solid-phase synthesized fluorescent lead-free organic–inorganic hybrid

compounds, *Journal of Materials Chemistry A*, 2019, **7**, 26504-26512.

76. W. Zhang, W. Zheng, L. Li, P. Huang, J. Xu, W. Zhang, Z. Shao and X. Chen, Unlocking the Potential of Organic-Inorganic Hybrid Manganese Halides for Advanced Optoelectronic Applications, *Advanced Materials*, 2024, **36**, 2408777.

77. Y. Rodríguez-Lazcano, L. Nataf and F. Rodríguez, Electronic structure and luminescence of ${[[{((\text{CH}}_{3}))}_{4}\text{N}]]}_{2}\text{Mn}{X}_{4}$ $(X=\text{Cl},\text{Br})$ crystals at high pressures by time-resolved spectroscopy: Pressure effects on the Mn-Mn exchange coupling, *Physical Review B*, 2009, **80**, 085115.

78. S. Zhang, K. Han and Z. Xia, Pseudohalide Anions Driven Structural Modulation in Distorted Tetrahedral Manganese(II) Hybrids Toward Tunable Green-Red Emissions, *Angewandte Chemie International Edition*, 2025, **64**, e202419333.

79. Z. Qi, K. Zhang, X. Zhao, N. Zhang, S.-L. Li and X.-M. Zhang, Promoting structural distortion to enhance the crystal field strength of Mn(ii) in tetrahedral bromide for near-unity yellow emission, *Chemical Communications*, 2024, **60**, 12880-12883.

80. Q. Ren, J. Zhang, Y. Mao, M. S. Molokeev, G. Zhou and X.-M. Zhang, Ligand Engineering Triggered Efficiency Tunable Emission in Zero-Dimensional Manganese Hybrids for White Light-Emitting Diodes, *Nanomaterials*, 2022, **12**, 3142.

81. F. Yu, S. Y. Li, H. R. Yang, J. Shen, M. X. Yin, Y. R. Tian, Y. T. Zhang, X. W. Kong and X. W. Lei, Crystal-Rigidifying Strategy in Hybrid Manganese Halide to Achieve Narrow Green Emission and High Structural Stability, *Inorganic Chemistry*, 2024, **63**, 14116-14125.

82. Y. Wang, T. Zhou, J. Chen, H. Qin, J. Wu, Z. Qin, H. Gu, Z. Gao, R. Liu, T. Ye, Y. Yang, F. Sun, T. Zhang, J. Hou, Y. Fang, Y. He, Y.-Y. Sun, M. Wang, L. Wang, H. Chen and W. Jiang, Flexible 3D printed fibers of novel manganese halides with superior acid/alkali resistance for X-ray imaging and radiation warning, *Chemical Engineering Journal*, 2025, **515**, 163495.

83. W. Li, Z. Zhou, C. Wang, Y. Li, S. Kurosawa, G. Ren, X. OuYang and Y. Wu, Red-Emitting Organic–Inorganic Hybrid Manganese(II) Halides for X-Ray Imaging, *Advanced Sensor Research*, 2023, **2**, 2200083.

84. X. Bai, H. Zhong, B. Chen, C. Chen, J. Han, R. Zeng and B. Zou, Pyridine-Modulated Mn Ion Emission Properties of C10H12N2MnBr4 and C5H6NMnBr3 Single Crystals, *The Journal of Physical Chemistry C*, 2018, **122**, 3130-3137.

85. X. Zhu, X. Yan, E. Kang, Y. Han, C. Yin and S. Ye, Suppressing Energy Migration via Antiparallel Spin Alignment in One-Dimensional Mn2+ Halide Magnets with High Luminescence Efficiency, *Angewandte Chemie International Edition*, 2025, **64**, e202417218.

86. H.-L. Xuan, Y.-F. Sang, L.-J. Xu, D.-S. Zheng, C.-M. Shi and Z.-N. Chen, Amino-Acid-Induced Circular Polarized Luminescence in One-Dimensional Manganese(II) Halide Hybrid, *Chemistry – A European Journal*, 2022, **28**, e202201299.

87. G. Hu, B. Xu, A. Wang, Y. Guo, J. Wu, F. Muhammad, W. Meng, C. Wang, S. Sui, Y. Liu, Y. Li, Y. Zhang, Y. Zhou and Z. Deng, Stable and Bright Pyridine Manganese Halides for Efficient White Light-Emitting Diodes, *Advanced Functional Materials*, 2021, **31**, 2011191.

88. Y. Zhang, W.-Q. Liao, D.-W. Fu, H.-Y. Ye, C.-M. Liu, Z.-N. Chen and R.-G. Xiong, The First Organic–Inorganic Hybrid Luminescent Multiferroic: (Pyrrolidinium)MnBr3, *Advanced Materials*, 2015, **27**, 3942-3946.

89. Y. Wu, X. Zhang, B. Zhang, L.-D. Xin, X.-M. Zhen and L.-J. Xu, Temperature/water triggered reversible emission transition in a one-dimensional Mn(ii)-based metal halide, *Journal of Materials Chemistry C*, 2024, **12**, 16471-16477.

90. X.-W. Kong, L.-X. Wu, X. Yang, D.-Y. Wang, S.-X. Wang, S.-Y. Li, C.-Y. Yue, F. Yu and X.-W. Lei, Enhancing the Water-Stability of 1D Hybrid Manganese Halides by a Cationic Engineering Strategy, *Advanced Optical Materials*, 2024, **12**, 2302710.

91. C. Li, X. Bai, Y. Guo and B. Zou, Tunable Emission Properties of Manganese Chloride Small Single Crystals by Pyridine Incorporation, *ACS Omega*, 2019, **4**, 8039-8045.

92. X.-H. Lv, W.-Q. Liao, P.-F. Li, Z.-X. Wang, C.-Y. Mao and Y. Zhang, Dielectric and photoluminescence properties of a layered perovskite-type organic–inorganic hybrid phase transition compound: NH3(CH2)5NH3MnCl4, *Journal of Materials Chemistry C*, 2016, **4**, 1881-1885.

93. D. Liang, H. Xiao, W. Cai, S. Lu, S. Zhao, Z. Zang and L. Xie, Mn2+-Based Luminescent Metal Halides: Syntheses, Properties, and Applications, *Advanced Optical Materials*, 2023, **11**, 2202997.

94. K. Li, W. Zhang, L. Niu, Y. Ye, J. Ren and C. Liu, Lead-Free Cesium Manganese Halide Nanocrystals Embedded Glasses for X-Ray Imaging, *Advanced Science*, 2023, **10**, 2204843.

95. Q. Kong, B. Yang, J. Chen, R. Zhang, S. Liu, D. Zheng, H. Zhang, Q. Liu, Y. Wang and K. Han, Phase Engineering of Cesium Manganese Bromides Nanocrystals with Color-Tunable Emission, *Angewandte Chemie International Edition*, 2021, **60**, 19653-19659.

96. S.-H. Xue, C.-M. Shi, L.-J. Xu and Z.-N. Chen, Thermal and Vapor Induced Triple-Mode Luminescent Switch of Manganese (II) Halides Hybrid, *Advanced Optical Materials*, 2024, **12**, 2302854.

97. X. Dai, Y. Deng, X. Peng and Y. Jin, Quantum-Dot Light-Emitting Diodes for Large-Area Displays: Towards the Dawn of Commercialization, *Advanced Materials*, 2017, **29**, 1607022.

98. X. Wang, Z. Bao, Y.-C. Chang and R.-S. Liu, Perovskite Quantum Dots for Application in High Color Gamut Backlighting Display of Light-Emitting Diodes, *ACS Energy Letters*, 2020, **5**, 3374-3396.

99. T. Hu, D. Li, Q. Shan, Y. Dong, H. Xiang, W. C. H. Choy and H. Zeng, Defect Behaviors in Perovskite Light-Emitting Diodes, *ACS Materials Letters*, 2021, **3**, 1702-1728.

100. R. K. Battula, C. Sudakar, P. Bhyrappa, G. Veerappan and E. Ramasamy, Single-Crystal Hybrid Lead Halide Perovskites: Growth, Properties, and Device Integration for Solar Cell Application, *Crystal Growth & Design*, 2022, DOI: 10.1021/acs.cgd.2c00789.

101. G. Kakavelakis, M. Gedda, A. Panagiotopoulos, E. Kymakis, T. D. Anthopoulos and K. Petridis, Metal Halide Perovskites for High-Energy Radiation Detection, *Advanced Science*, 2020, **7**, 2002098.

102. S. Liu, B. Yang, J. Chen, D. Wei, D. Zheng, Q. Kong, W. Deng and K. Han, Efficient Thermally Activated Delayed Fluorescence from All-Inorganic Cesium Zirconium Halide

Perovskite Nanocrystals, *Angewandte Chemie International Edition*, 2020, **59**, 21925-21929.

103. C. Fang, J. Yang, G. Zhou, Z. Zhang, Y. Mao, X. Yun, L. Liu, D. Xu, X. Li and J. Zhou, Energy transfer from self-trapped excitons to rare earth ions in Cs2ZrCl6 perovskite variants, *Journal of Materials Chemistry C*, 2023, **11**, 1095-1102.

104. H. Peng, X. He, Q. Wei, Y. Tian, W. Lin, S. Yao and B. Zou, Realizing High-Efficiency Yellow Emission of Organic Antimony Halides via Rational Structural Design, *ACS Applied Materials & Interfaces*, 2022, DOI: 10.1021/acsami.2c14169.

105. C. Zhou, H. Lin, Y. Tian, Z. Yuan, R. Clark, B. Chen, L. J. van de Burgt, J. C. Wang, Y. Zhou, K. Hanson, Q. J. Meisner, J. Neu, T. Besara, T. Siegrist, E. Lambers, P. Djurovich and B. Ma, Luminescent zero-dimensional organic metal halide hybrids with near-unity quantum efficiency, *Chemical Science*, 2018, **9**, 586-593.

106. Z. Li, Y. Li, P. Liang, T. Zhou, L. Wang and R.-J. Xie, Dual-Band Luminescent Lead-Free Antimony Chloride Halides with Near-Unity Photoluminescence Quantum Efficiency, *Chemistry of Materials*, 2019, **31**, 9363-9371.

107. M. Leng, Y. Yang, Z. Chen, W. Gao, J. Zhang, G. Niu, D. Li, H. Song, J. Zhang, S. Jin and J. Tang, Surface Passivation of Bismuth-Based Perovskite Variant Quantum Dots To Achieve Efficient Blue Emission, *Nano Letters*, 2018, **18**, 6076-6083.

108. J.-H. Wei, J.-F. Liao, X.-D. Wang, L. Zhou, Y. Jiang and D.-B. Kuang, All-Inorganic Lead-Free Heterometallic Cs4MnBi2Cl12 Perovskite Single Crystal with Highly Efficient Orange Emission, *Matter*, 2020, **3**, 892-903.

109. T. Jun, K. Sim, S. Iimura, M. Sasase, H. Kamioka, J. Kim and H. Hosono, Lead-Free Highly Efficient Blue-Emitting Cs3Cu2I5 with 0D Electronic Structure, *Advanced Materials*, 2018, **30**, 1804547.

110. J. Luo, M. Hu, G. Niu and J. Tang, Lead-Free Halide Perovskites and Perovskite Variants as Phosphors toward Light-Emitting Applications, *ACS Applied Materials & Interfaces*, 2019, **11**, 31575-31584.

111. K. M. McCall, K. Sakhatskyi, E. Lehmann, B. Walfort, A. S. Losko, F. Montanarella, M. I. Bodnarchuk, F. Krieg, Y. Kelestemur, D. Mannes, Y. Shynkarenko, S. Yakunin and M. V. Kovalenko, Fast Neutron Imaging with Semiconductor Nanocrystal Scintillators, *ACS Nano*, 2020, **14**, 14686-14697.

112. J. Cao, Z. Guo, S. Zhu, Y. Fu, H. Zhang, Q. Wang and Z. Gu, Preparation of Lead-free Two-Dimensional-Layered (C8H17NH3)2SnBr4 Perovskite Scintillators and Their Application in X-ray Imaging, *ACS Applied Materials & Interfaces*, 2020, **12**, 19797-19804.

113. W. Zhu, W. Ma, Y. Su, Z. Chen, X. Chen, Y. Ma, L. Bai, W. Xiao, T. Liu, H. Zhu, X. Liu, H. Liu, X. Liu and Y. Yang, Low-dose real-time X-ray imaging with nontoxic double perovskite scintillators, *Light: Science & Applications*, 2020, **9**, 112.

114. B. Yang, L. Yin, G. Niu, J.-H. Yuan, K.-H. Xue, Z. Tan, X.-S. Miao, M. Niu, X. Du, H. Song, E. Lifshitz and J. Tang, Lead-Free Halide Rb2CuBr3 as Sensitive X-Ray Scintillator, *Advanced Materials*, 2019, **31**, 1904711.

115. Y. Yu, Y. Tang, B. Wang, K. Zhang, J.-X. Tang and Y.-Q. Li, Red Perovskite Light-Emitting Diodes: Recent Advances and Perspectives, *Laser & Photonics Reviews*, 2023, **17**, 2200608.

116. K.-H. Jin, Y. Zhang, K.-J. Li, M.-E. Sun, X.-Y. Dong, Q.-L. Wang and S.-Q. Zang, Enantiomorphic Single Crystals of Linear Lead(II) Bromide Perovskitoids with White Circularly Polarized Emission, *Angewandte Chemie International Edition*, 2022, **61**, e202205317.

117. J. Ma, C. Fang, C. Chen, L. Jin, J. Wang, S. Wang, J. Tang and D. Li, Chiral 2D Perovskites with a High Degree of Circularly Polarized Photoluminescence, *ACS Nano*, 2019, **13**, 3659-3665.

118. J. Wang, C. Fang, J. Ma, S. Wang, L. Jin, W. Li and D. Li, Aqueous Synthesis of Low-Dimensional Lead Halide Perovskites for Room-Temperature Circularly Polarized Light Emission and Detection, *ACS Nano*, 2019, **13**, 9473-9481.

119. F. Wang, X. Li, T. Chen, L. Wang, C. Li, W. Zhang, W. Yuan, S. Lu, L. Li and X. Chen, A strategy of chiral cation coordination to achieve a large luminescence dissymmetry factor in 1D hybrid manganese halides, *Chemical Science*, 2025, DOI: 10.1039/D5SC01615K.

120. M. P. Davydova, L. Meng, M. I. Rakhmanova, Z. Jia, A. S. Berezin, I. Y. Bagryanskaya, Q. Lin, H. Meng and A. V. Artem'ev, Strong Magnetically-Responsive Circularly Polarized Phosphorescence and X-Ray Scintillation in Ultrarobust Mn(II)–Organic Helical Chains, *Advanced Materials*, 2023, **35**, 2303611.

121. J. Chen, S. Zhang, X. Pan, R. Li, S. Ye, A. K. Cheetham and L. Mao, Structural Origin of Enhanced Circularly Polarized Luminescence in Hybrid Manganese Bromides, *Angewandte Chemie International Edition*, 2022, **61**, e202205906.

122. C. Li, Y. Wei, Y. Li, Z. Luo, Y. Liu, M. He, Y. Zhang, X. He, X. Chang and Z. Quan, Manipulating Chiroptical Activities in 0D Chiral Hybrid Manganese Bromides by Solvent Molecular Engineering, *Small*, 2024, **20**, 2400338.

123. Y. Zhang, R. Sun, X. Ou, K. Fu, Q. Chen, Y. Ding, L.-J. Xu, L. Liu, Y. Han, A. V. Malko, X. Liu, H. Yang, O. M. Bakr, H. Liu and O. F. Mohammed, Metal Halide Perovskite Nanosheet for X-ray High-Resolution Scintillation Imaging Screens, *ACS Nano*, 2019, **13**, 2520-2525.

124. Q. Kong, X. Meng, S. Ji, Q. Wang, B. Yang, T. Bai, X. Wang, Z. Wang, R. Zhang, D. Zheng, F. Liu and K.-l. Han, Highly Reversible Cesium Manganese Iodine for Sensitive Water Detection and X-ray Imaging, *ACS Materials Letters*, 2022, **4**, 1734-1741.

125. K. Han, K. Sakhatskyi, J. Jin, Q. Zhang, M. V. Kovalenko and Z. Xia, Seed-Crystal-Induced Cold Sintering Toward Metal Halide Transparent Ceramic Scintillators, *Advanced Materials*, 2022, **34**, 2110420.

126. H. Wei, Y. Fang, P. Mulligan, W. Chuirazzi, H.-H. Fang, C. Wang, B. R. Ecker, Y. Gao, M. A. Loi, L. Cao and J. Huang, Sensitive X-ray detectors made of methylammonium lead tribromide perovskite single crystals, *Nature Photonics*, 2016, **10**, 333-339.

127. W. Ma, T. Jiang, Z. Yang, H. Zhang, Y. Su, Z. Chen, X. Chen, Y. Ma, W. Zhu, X. Yu, H. Zhu, J. Qiu, X. Liu, X. Xu and Y. Yang, Highly Resolved and Robust Dynamic X-Ray Imaging Using Perovskite Glass-Ceramic Scintillator with Reduced Light Scattering, *Advanced Science*, 2021, **8**, 2003728.

128. R. Chiara, M. Morana, M. Boiocchi, M. Coduri, M. Striccoli, F. Fracassi, A. Listorti, A. Mahata, P. Quadrelli, M. Gaboardi, C. Milanese, L. Bindi, F. De Angelis and L. Malavasi, Role of spacer cations and structural distortion in two-dimensional

Chemical Science Accepted Manuscript

germanium halide perovskites, *Journal of Materials Chemistry C*, 2021, **9**, 9899-9906.

129. B.-R. Hyun, C.-W. Sher, Y.-W. Chang, Y. Lin, Z. Liu and H.-C. Kuo, Dual Role of Quantum Dots as Color Conversion Layer and Suppression of Input Light for Full-Color Micro-LED Displays, *The Journal of Physical Chemistry Letters*, 2021, **12**, 6946-6954.

130. S. Ji, X. Yuan, J. Li, J. Hua, Y. Wang, R. Zeng, H. Li and J. Zhao, Photoluminescence Lifetimes and Thermal Degradation of Mn2+-Doped CsPbCl3 Perovskite Nanocrystals, *The Journal of Physical Chemistry C*, 2018, **122**, 23217-23223.

131. S. Das Adhikari, S. K. Dutta, A. Dutta, A. K. Guria and N. Pradhan, Chemically Tailoring the Dopant Emission in Manganese-Doped CsPbCl3 Perovskite Nanocrystals, *Angewandte Chemie International Edition*, 2017, **129**, 8872-8876.

132. W. Liu, J. Zheng, S. Cao, L. Wang, F. Gao, K.-C. Chou, X. Hou and W. Yang, Mass production of Mn2+-doped CsPbCl3 perovskite nanocrystals with high quality and enhanced optical performance, *Inorganic Chemistry Frontiers*, 2018, **5**, 2641-2647.

133. Y. Li, C. Wang, G. Hu, W. Meng, S. Sui and Z. Deng, Promoting the doping efficiency and photoluminescence quantum yield of Mn-doped perovskite nanocrystals via two-step hot-injection, *Chemical Communications*, 2022, **58**, 941-944.

134. K. Xing, X. Yuan, Y. Wang, J. Li, Y. Wang, Y. Fan, L. Yuan, K. Li, Z. Wu, H. Li and J. Zhao, Improved Doping and Emission Efficiencies of Mn-Doped CsPbCl3 Perovskite Nanocrystals via Nickel Chloride, *The Journal of Physical Chemistry Letters*, 2019, **10**, 4177-4184.

135. J. Zhu, X. Yang, Y. Zhu, Y. Wang, J. Cai, J. Shen, L. Sun and C. Li, Room-Temperature Synthesis of Mn-Doped Cesium Lead Halide Quantum Dots with High Mn Substitution Ratio, *The Journal of Physical Chemistry Letters*, 2017, **8**, 4167-4171.

136. D. Chen, G. Fang, X. Chen, L. Lei, J. Zhong, Q. Mao, S. Zhou and J. Li, Mn-Doped CsPbCl3 perovskite nanocrystals: solvothermal synthesis, dual-color luminescence and improved stability, *Journal of Materials Chemistry C*, 2018, **6**, 8990-8998.

137. K. Xu, C. C. Lin, X. Xie and A. Meijerink, Efficient and Stable Luminescence from Mn2+ in Core and Core–Isocrystalline Shell CsPbCl3 Perovskite Nanocrystals, *Chemistry of Materials*, 2017, **29**, 4265-4272.

138. W. J. Mir, M. Jagadeeswararao, S. Das and A. Nag, Colloidal Mn-Doped Cesium Lead Halide Perovskite Nanoplatelets, *ACS Energy Letters*, 2017, **2**, 537-543.

139. Z.-J. Li, E. Hofman, A. H. Davis, A. Khammang, J. T. Wright, B. Dzikovski, R. W. Meulenberg and W. Zheng, Complete Dopant Substitution by Spinodal Decomposition in Mn-Doped Two-Dimensional CsPbCl3 Nanoplatelets, *Chemistry of Materials*, 2018, **30**, 6400-6409.

140. Z. L. He, J. H. Wei, Z. Z. Zhang, J. B. Luo and D. B. Kuang, Manganese-Halide Single-Crystal Scintillator Toward High-Performance X-Ray Detection and Imaging: Influences of Halogen and Thickness, *Advanced Optical Materials*, 2023, **11**, 2300449.

141. W. Zhang, P. Sui, W. Zheng, L. Li, S. Wang, P. Huang, W. Zhang, Q. Zhang, Y. Yu and X. Chen, Pseudo-2D Layered Organic-Inorganic Manganese Bromide with a Near-Unity Photoluminescence Quantum Yield for White Light-Emitting Diode and X-Ray Scintillator, *Angewandte Chemie International Edition*, 2023, **62**, e202309230.

142. W. Shao, G. Zhu, X. Wang, Z. Zhang, H. Lv, W. Deng, X. Zhang and H. Liang, Highly Efficient, Flexible, and Eco-Friendly Manganese(II) Halide Nanocrystal Membrane with Low Light Scattering for High-Resolution X-ray Imaging, *ACS Applied Materials & Interfaces*, 2023, **15**, 932-941.
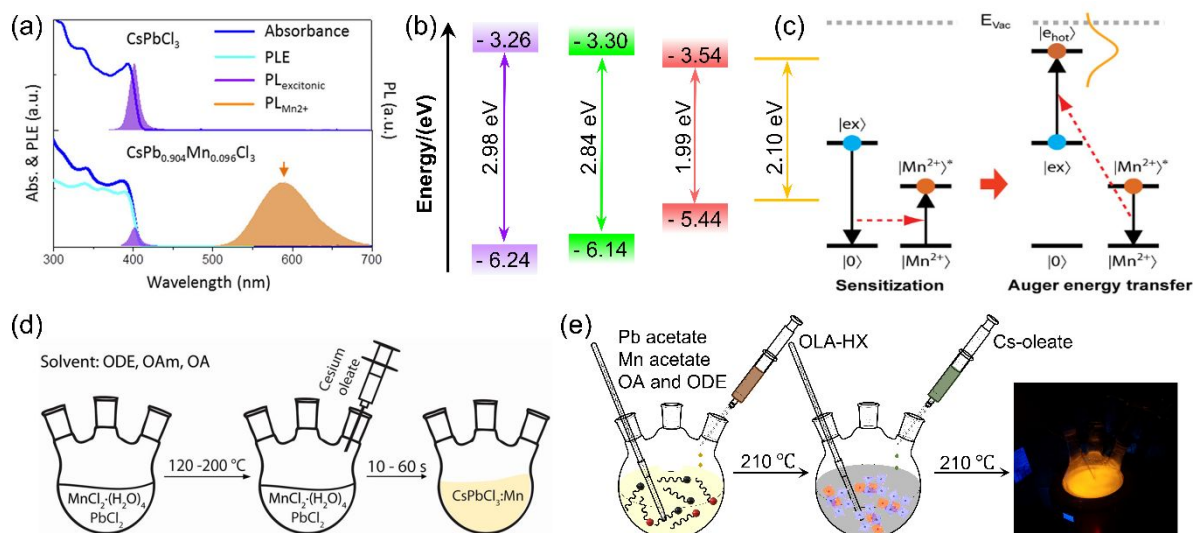
ARTICLE

Figure 1. (a) The optical properties of undoped (top) and Mn-doped (bottom) CsPbCl$_3$ NCs. (b) Band gap structure of CsPbX$_3$ and Mn d-states. (c) Photophysical pathways of hot electron up-conversion. |0⟩ and |ex⟩ are ground and exciton states of the host NCs. |Mn^{2+}⟩ and |Mn^{2+}⟩* are ground and excited states of dopants. |e$_{hot}$⟩ represents the state generating hot electrons. E$_{vac}$ is the vacuum level. Schematic diagram of the synthesis of Mn-doped CsPbX$_3$ NCs via (d) one-step hot injection and (e) two-step hot-injection process. (a) Reproduced with permission from Ref.[15]. Copyright 2016, American Chemistry Society. (c) Reproduced with permission from Ref.[34]. Copyright 2021, American Chemistry Society. (d) Reproduced with permission from Ref.[14]. Copyright 2016, American Chemistry Society.
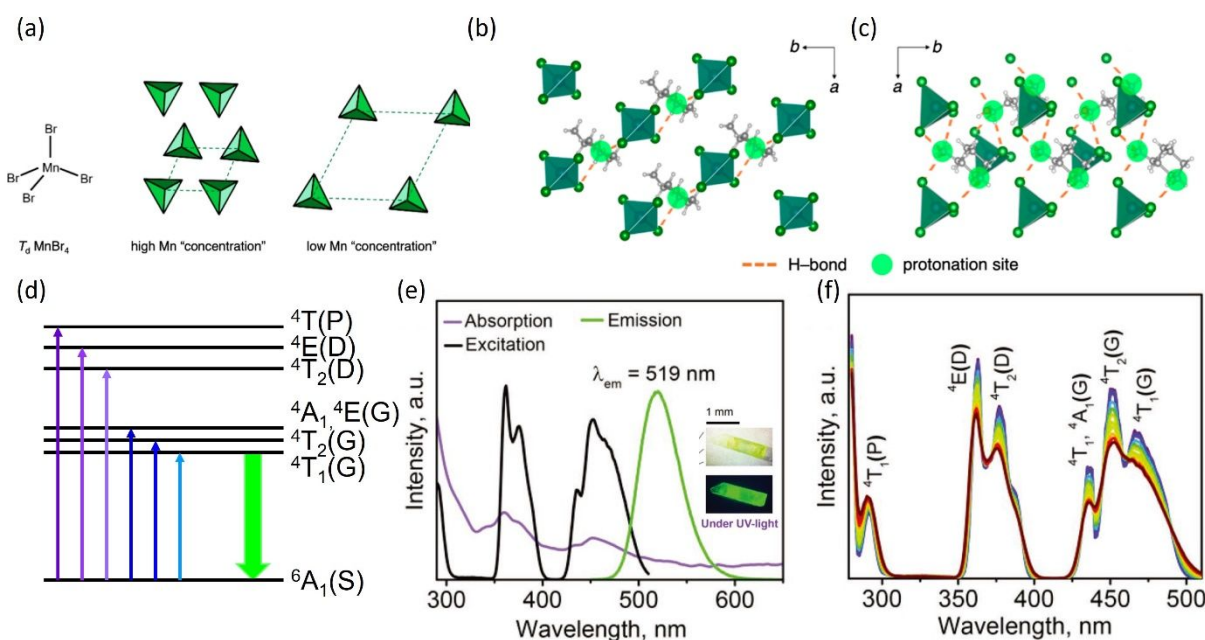

Figure 2. Structure and luminescent properties of four fold coordinated [MnX$_4$]$^{2-}$ complexes. (a) Illustration of manganese bromide in tetrahedral environment with short Mn-Mn distances (high Mn "concentration") and long Mn-Mn distances (low Mn "concentration"). (b) Crystal structure of A$_2$MnX$_4$ with +1 cation. (c) Crystal structure of AMnX$_4$ with +2 cation. (d) Schematic diagram showing the emission mechanism of green emissive Mn(Ⅱ) halide complexes. (e) Absorption, steady-state PLE and PL spectra at 298 K and (f) temperature-dependent PLE spectra of 1R/1S Mn(Ⅱ) halide complexes. (a)(b)(c) Reproduced with permission from Ref.[62]. Copyright 2020, American Chemistry Society. (e, f) Reproduced with permission from Ref.[65]. Copyright 2023, Wiley-VCH.
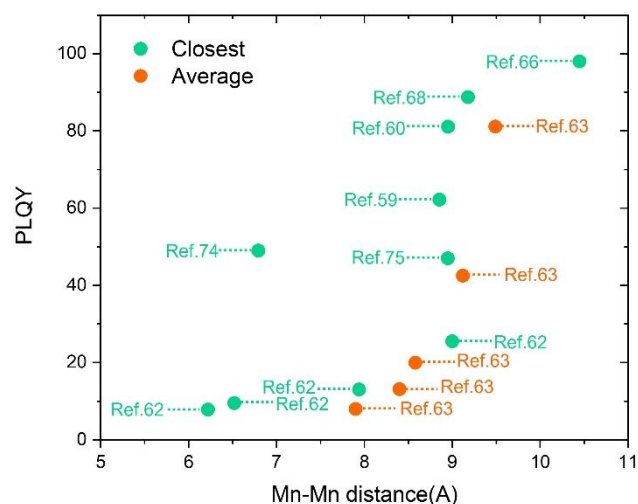
Figure 3. Correlation between shortest Mn-Mn distances and PLQY. Red scatters represent samples evaluated via average Mn-Mn distance and black scatters represent samples evaluated via closest Mn-Mn distance.
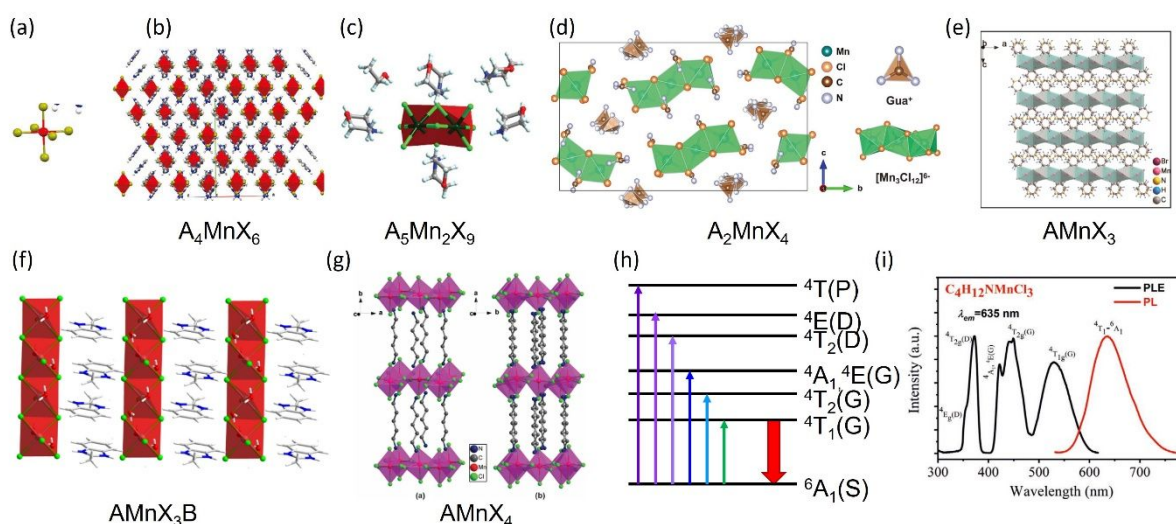

Figure 4. Structural configurations of octahedral [MnX$_6$]$^{4-}$ complexes in Mn(II) halides. (a) Schematic representation of the fundamental [MnX$_6$]$^{4-}$ coordination unit. (b) Zero-dimensional (0D) structure featuring isolated [MnX$_6$]$^{4-}$ octahedra (exemplified by A$_4$MnX$_6$). (c) 0D structure containing face-sharing [Mn$_2$X$_9$]$^{5-}$ units (represented by A$_5$Mn$_2$X$_9$). (d) 0D structure with face-sharing [Mn$_3$X$_{12}$]$^{6-}$ units (A$_2$MnX$_4$). (e) One-dimensional (1D) chain structure composed of face-sharing octahedra (AMnX$_3$). (f) 1D chain structure with edge-sharing octahedra (AMnX$_3$B). (g) Two-dimensional (2D) layered structure (AMnX$_4$). (h) Schematic diagram showing the emission mechanism of red emissive Mn(Ⅱ) halide complexes. (i) PLE and PL spectra of C$_4$H$_{12}$NMnX$_3$ Mn(Ⅱ) halide complexes. (a,b) Reproduced with permission from Ref.[17]. Copyright 2021, Wiley-VCH. (c) Reproduced with permission from Ref.[61]. Copyright 2019, Royal Society of Chemistry. (d) Reproduced with permission from Ref.[83]. Copyright 2021, Wiley-VCH. (e) Reproduced with permission from Ref.[84]. Copyright 2018, Royal Society of Chemistry. (f) Reproduced with permission from Ref.[21]. Copyright 2024, American Chemical Society. (g) Reproduced with permission from Ref.[92]. Copyright 2016, American Chemical Society. (i) Reproduced with permission from Ref.[16]. Copyright 2021, Wiley-VCH.
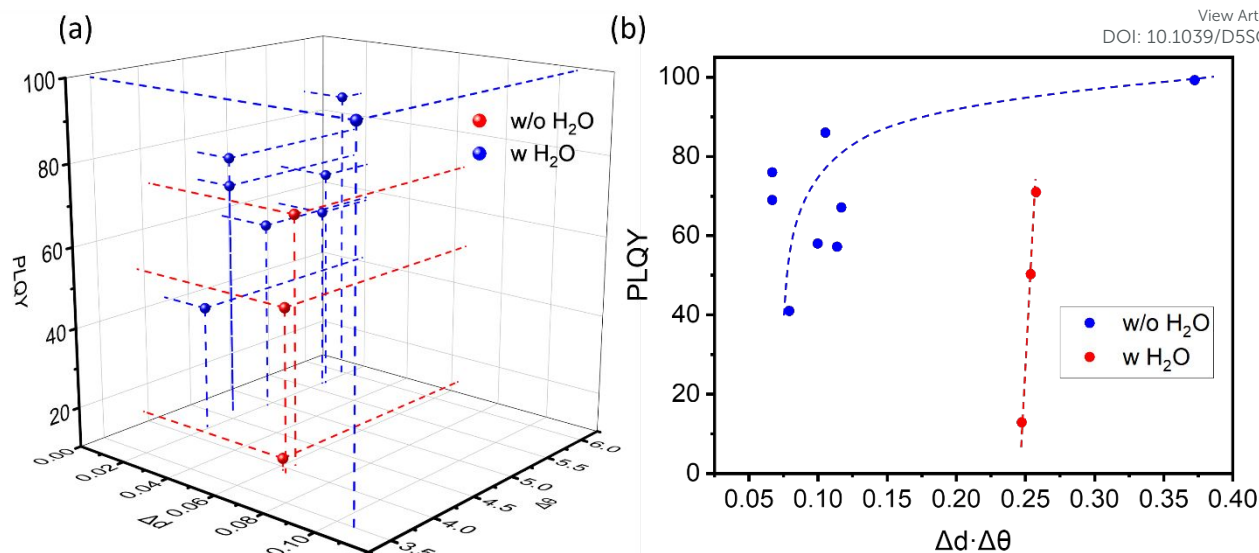
Figure 5. PLQY and structure. (a) PLQY with Mn-X distance distortion (Δd) and X-Mn-X angle distortion ($\Delta\theta$). (b) PLQY with composite parameter $\Delta d \cdot \Delta\theta$.
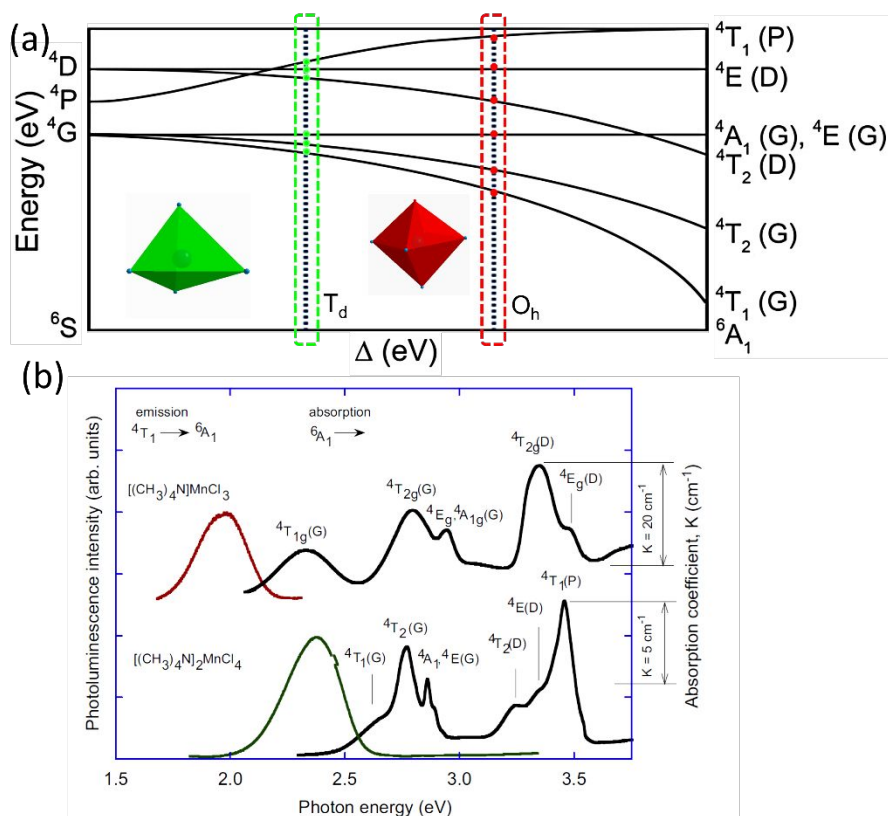

Figure 6. (a) Tanabe–Sugano diagrams for Mn^{2+} ($3d^5$). (b) PL and PLE of green $[(CH_3)_4N]_2MnCl_4$ and red $[(CH_3)_4N]MnCl_3$. (a) Reproduced with permission from Ref.[58]. Copyright 2021, Wiley-VCH. (b) Reproduced with permission from Ref.[73]. Copyright 2009, Elsevier.
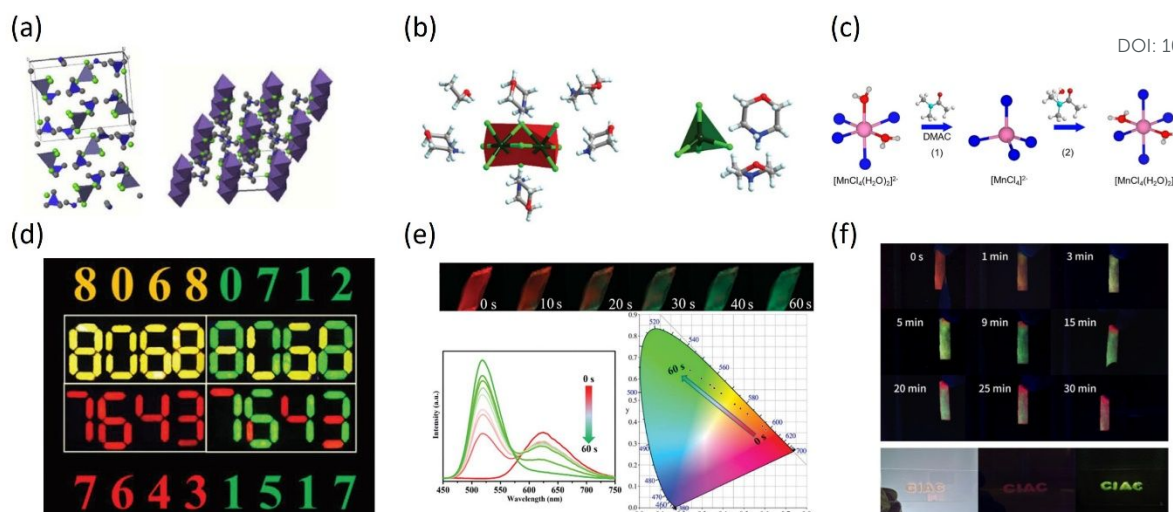
Chemical Science Accepted Manuscript

Figure 7. Structure and luminescent properties of Mn(Ⅱ) halide complexes with phase regulation between red and green emission. (a) Crystal structure of green $(C_5H_6N)_2MnBr_4$ and red $C_5H_6NMnBr_3$. (b) Crystal structure of $(C_4NOH_{10})_5Mn_2Cl_9 \cdot C_2H_5OH$ and $(C_4NOH_{10})_2MnCl_4$. (c) Phase regulation between $Cs_2[MnX_4(H_2O)_2]$ and Cs_2MnX_4. (d) Photographs of the water-induced phase transformation process of $CsMnBr_3:Pb^{2+}$ NCs under 365 nm UV light. (e) Thermo-chromic luminescence of $(C_4NOH_{10})_5Mn_2Cl_9 \cdot C_2H_5OH$ and $(C_4NOH_{10})_2MnCl_4$ under thermal treatment. (f) Photographs of test strips loaded with $Cs_2[MnX_4(H_2O)_2]$ powder after adding DMAC. (a) Reproduced with permission from Ref.[73]. Copyright 2009, Elsevier. (b, e) Reproduced with permission from Ref.[61]. Copyright 2019, Royal Society of Chemistry. (d) Reproduced with permission from Ref.[96]. Copyright 2024, Wiley-VCH. (c, f) Reproduced with permission from Ref.[58]. Copyright 2020, Wiley-VCH.
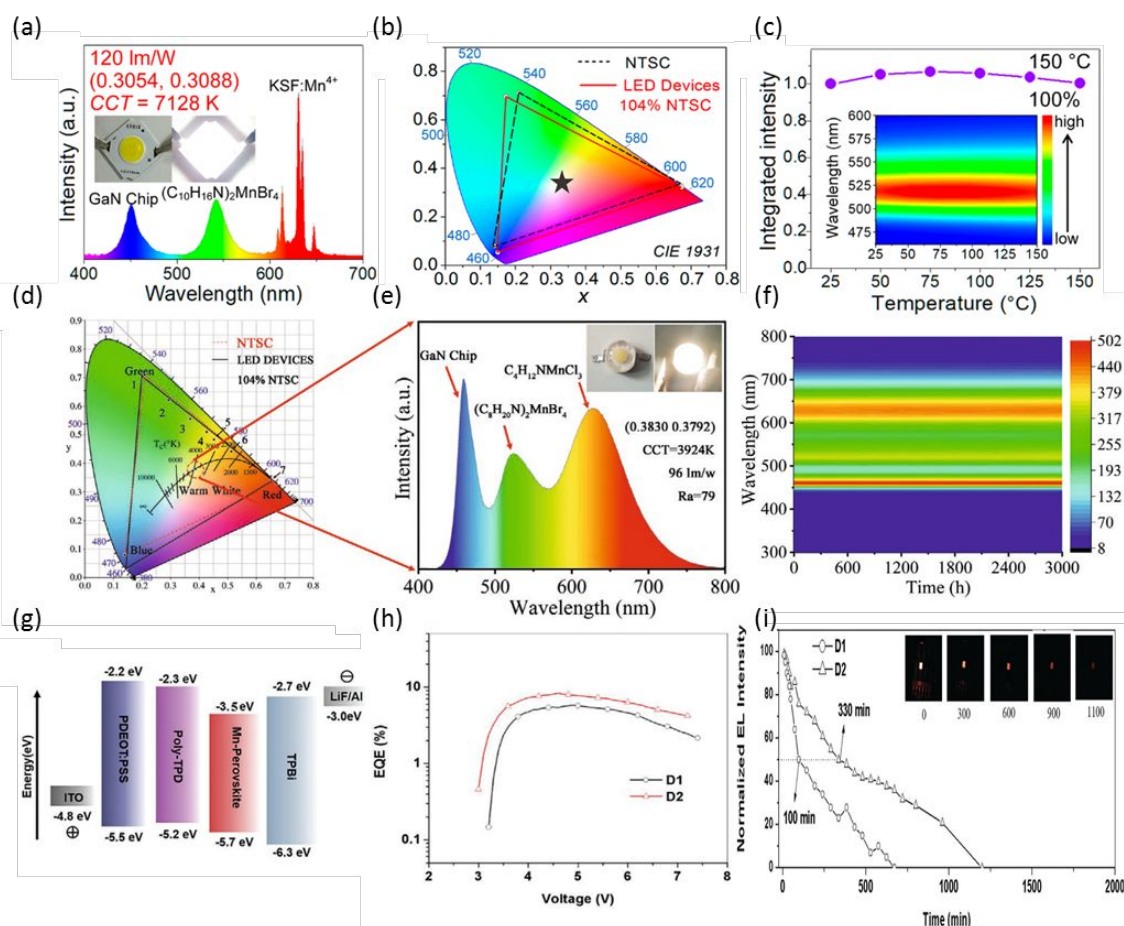

Figure 8. Luminescent and stability properties of LEDs with Mn(Ⅱ) halide complexes. (a) Emission spectrum of the white LED fabricated with $(C_{10}H_{16}N)_2MnBr_4$ and the $K_2SiF_6:Mn^{4+}$ phosphors on the InGaN chip (λem = 450 nm) at a 20 mA. The insets show the photographs of device. (b) Color gamut of NTSC standard (black dotted line) and the fabricated white LED (red line, 104%) in the CIE 1931 system. (c) Integrated PL intensity of $(C_{10}H_{16}N)_2MnBr_4$ as a function of temperature. (d) Color gamut of NTSC standard (red dotted line) and the fabricated white LED (black line, 104%) in the CIE 1931 system. (e) Emission spectrum of the white LED using blending of $C_4H_{12}NMnCl_3$ and $(C_8H_{20}N)_2MnBr_4$ with InGaN chip (λem = 460 nm). The inset shows the photograph of the LED device with power off and on. (f) Integrated emission spectrum intensity of white LED under operation as a function of time. (g) Bandgaps of the $(ABI)_4MnBr_6$ EL-LED. (h) EQEs of $(ABI)_4MnBr_6$ EL-LEDs at different voltages. (i) Stability of $(ABI)_4MnBr_6$ EL-LED with a voltage of 5.0 V. (a,b,c) Reproduced with

permission from Ref. [68]. Copyright 2020, American Chemical Society. (d,e,f) Reproduced with permission from Ref.[16]. Copyright 2021, Wiley-VCH. (g,h,i) Reproduced with permission from Ref.[17]. Copyright 2021, Wiley-VCH.
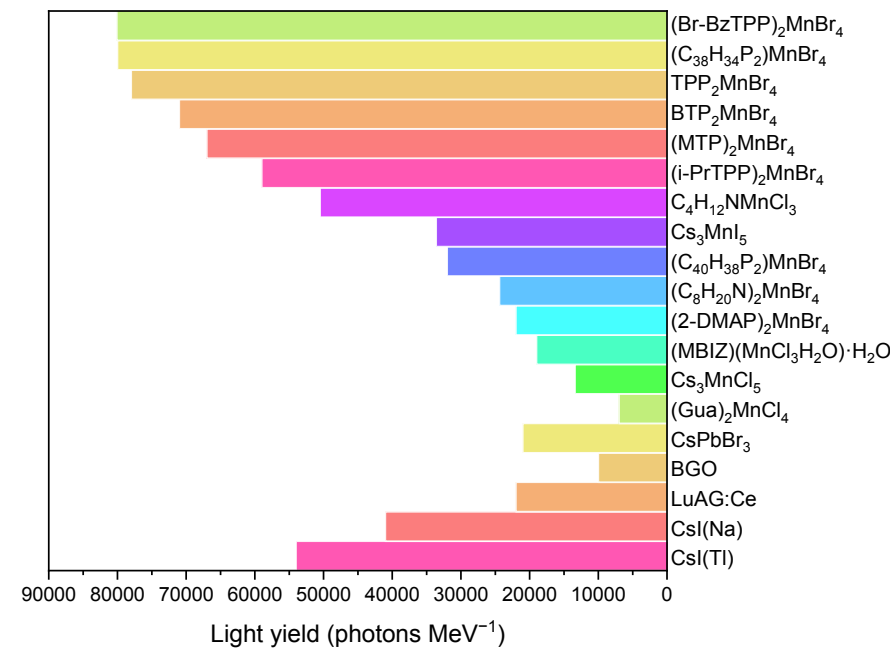
Figure 9. Comparison of scintillator light yields of various Mn(Ⅱ) complexes and previously reported and commercially available scintillators.

Table 1. Synthesis Information of Mn-Doped Perovskite Nanocrystals.

Materials	Precursors	Mn: Pb	Temp/°C	Method	Doping/%	QY/%	Reference
CsPbCl₃: Mn NCs	$MnCl_2$, $PbCl_2$, TOP	2.5: 1	185	Hot injection	9.6	27	15
	$MnCl_2$, $PbCl_2$, TOP	0.4: 1	185	Hot injection	12	27	40
	$MnCl_2$, $PbCl_2$, TOP	2: 1	150	Hot injection	3.1	58.8	130
	$MnCl_2$, $PbCl_2$, TOP, RNH_3Cl	0.05: 1	180	Hot injection	1.3	27	131
	$MnCl_2$, $PbCl_2$, TOP, RNH_3Cl	1: 1	190	Microwave	6.5	65	132
	$MnOAc_2$, $PbOAc_2$, RNH_3Cl	0.4: 1	210	Hot injection	17.3	84.4	133
	$MnCl_2$, $PbCl_2$, TOP, $CuCl_2$	0.2: 1	260	Hot injection	2	68	50
	$MnCl_2$, $PbCl_2$, TOP, $NiCl_2$	1: 1	190	Hot injection	1.97	70	134
	$MnCl_2$, $PbCl_2$	1.4: 1	200	Hot injection	0.2	60	14
	$MnCl_2$, $PbCl_2$	10: 1	170	Hot injection	27	54	35
	$MnCl_2$, $PbCl_2$	0.6: 1	150	Hot injection	5.8	12.7	42
	$MnCl_2$, $PbCl_2$	5: 1	RT	LARP	28	41	135
	$MnCl_2$, $PbCl_2$	0.6: 1	200	Solvothermal	1	64.2	136
	$MnCl_2$, $PbCl_2$	3: 1	RT	Ultrasonication	3	26	44
	$MnCl_2$, $PbCl_2$	2: 1	RT	Ultrasonication	11.8	41.1	41
	$MnOAc_2$, $PbCl_2$, TMS-Cl	1: 1	170	Hot injection	10.3	35	49
	$MnOAc_2$, $PbOAc_2$, HCl	0.1: 1	RT	LARP	1.0	40	137
CsPbCl₃: Mn NPLs	$MnCl_2$, $PbCl_2$	0.05: 1	RT	LARP	0.8	20	138
	$MnCl_2$, $PbCl_2$	1: 1	230	Hot injection	50.4	36	38
	$MnCl_2$, $PbCl_2$	0.8: 1	200	Solvothermal	8.8	20.8	139

Journal Name

ARTICLE

Table 2. Comparisons of red Mn(Ⅱ) complex in structure and luminescent properties.

sample	dimension	peak/nm	PLQY/%	Stokes shift/nm	closest Mn-Mn distance/Å	Δd/Å	Δθ/°	Ref
$(CH_6N_3)_2MnCl_4$	0D	642	69 / 76	125	3.323	0.0057	4.65	83, 85
$(ABI)_4MnBr_6$	0D	629	80	289	8.642	0.0086	/	17
$(ABI)_4MnCl_6$	0D	630	99	370	/	0.0413	3.50	82
$(MBI)MnCl_4·H_2O$	1D	650	50	300	/	0.0260	3.93	
$(MBZI)(MnCl_3H_2O)·H_2O$	1D	632	71	181	/	0.0253	4.09	21
$(C_8H_9N_2)_n\{(MnCl_3(H_2O) · H_2O)\}_n$	1D	645	13	200	3.645	0.0251	3.95	89
$(TMSO)MnCl_3$	1D	629	86	~179	3.243	0.0069	6.00	90
$(TMSO)MnBr_3$	1D	626	58	~176	3.377	0.0075	4.93	
$D-(C_9H_{17}NO_2)[MnCl_3]$	1D	646	67	/	3.213	0.0081	5.69	86
$L-(C_9H_{17}NO_2)[MnCl_3]$	1D	656	57	/	3.210	0.0079	5.65	
$CsMnCl_3$	1D	644-665	42	/	4.1	0.0074	4.23	94

Table 3. Comparisons of Mn(Ⅱ) complex scintillators in light yield, detection limit, spatial resolution and afterglow.

Material	Light yield/photons MeV^{-1}	Detection limit	Spatial resolution/ lp mm^{-1}	Afterglow	Reference
$S-[MBA-Me_3]MnBr_4$	/	320 μGy s^{-1}	/	/	65
$(Gua)_2MnCl_4$	7 000	145.3 nGy s^{-1}	8	BGO<$(Gua)_2MnCl_4$<CsI(Tl)	83
Cs_3MnCl_5	13 400	470 μGy s^{-1}	4.0	/	94
$(MBIZ)(MnCl_3H_2O)·H_2O$	19 000	204 nGy s^{-1}	11.1	30 ms(1%)	21
$(2-DMAP)_2MnBr_4$	22 000	9.5 nGy s^{-1}	20–25	/	140
$(C_8H_{20}N)_2MnBr_4$	24 400	24.2 nGyair s^{-1}	5	2.06 ms(1%)	16
$(C_{40}H_{38}P_2)MnBr_4$	32 000	288 nGy s^{-1}	/	~BGO	69
Cs_3MnI_5	33 600	400 nGy s^{-1}	7.45	/	124
$C_4H_{12}NMnCl_3$	50 500	36.9 nGyair s^{-1}	/	3.14 ms (1%)	16
$(i-PrTPP)_2MnBr_4$	59 000	42.3 nGyair s^{-1}	46.6	/	72
$(MTP)_2MnBr_4$	67 000	28.1 nGyair s^{-1}	6.2	/	141
BTP_2MnBr_4	71 000	86.2 nGyair s^{-1}	23.8	/	142
TPP_2MnBr_4	78 000±2 000	8.8 nGy s^{-1}	15.7	3 ms (0.5%)	125
$(C_{38}H_{34}P_2)MnBr_4$	80 000	72.8 nGy s^{-1}	~3	10 ms (to the background)	19
$(Br-BzTPP)_2MnBr_4$	80 100	30 nGy s^{-1}	14.06	0.3 ms to baseline	71

This journal is © The Royal Society of Chemistry 20xx

Data availability statements

No primary research results, software or code have been included and no new data were generated or analysed as part of this Perspective.

Chemical Science Accepted Manuscript